Universidade do Minho
Escola de Ciências

João Miguel Peixoto Oliveira

Modelização de Espectros de Raios-X em Filmes Finos

outubro de 2017

UMinho|2017 João Miguel Peixoto Oliveira **Modelização de Espectros de Raios-X em Filmes Finos**

Universidade do Minho
Escola de Ciências

João Miguel Peixoto Oliveira

Modelização de Espectros de Raios-X em Filmes Finos

Dissertação de Mestrado
Mestrado em Física
Ramo de Física Aplicada

Trabalho realizado sob orientação do
Professor Doutor Bernardo Gonçalves Almeida

outubro de 2017

DECLARATION

Nome: João Miguel Peixoto Oliveira

Endereço electrónico: pg22595@alunos.uminho.pt
Telefone: (H) (+351) 253 321 371 · (M) (+351) 918 206 264
Número do Cartão de cidadão: 13 974 167

Título dissertação: Modelização de Espectros de Raios-X em Filmes Finos

Orientador: Professor Doutor Bernardo Gonçalves Almeida

Ano de conclusão: 2017

Designação do Mestrado: Mestrado em Física - Ramo de Física Aplicada

É AUTORIZADA A REPRODUÇÃO INTEGRAL DESTA TESE / TRABALHO APENAS PARA EFEITOS DE INVESTIGAÇÃO, MEDIANTE DECLARAÇÃO ESCRITA DO INTERESSADO, QUE A TAL SE COMPROMETE.

Universidade do Minho, Outubro 2017

João Miguel Peixoto Oliveira

ABSTRACT

Thin film multilayers are layered structures composed of several different materials and are commonly prepared for specifically envisaged applications. X-ray diffraction is a nondestructive technique particularly suited for studying their structural properties. However, extracting structural parameters from X-ray diffraction, such as spacing between individual atomic planes, interlayer roughness or strain, requires modelling and fitting the X-ray diffraction spectra.

Here, we present a general kinematical model for wide angle X-ray diffraction of thin films that includes both the average atomic structure of the layers and structural disorder, for fitting the measured X-ray diffraction spectra. This model allows the extraction of composition (layer thicknesses), intralayer disorder and interfacial strain at the atomic scale that is assumed to be cumulative throughout the multilayer. In addition to the kinematical model, we also used an optical model for small angle X-ray reflectometry that allows us to obtain the composition (layer thicknesses and electronic density) and interfacial roughness. Unlike simpler fits of X-ray diffractograms that use functions like Gaussian, Lorentzian, or pseudo-Voigt, this model allows a more complete and accurate determination of the structure parameters.

By fitting the measured profiles, it is possible to quantitatively determine both lattice constants and disorder parameters of a wide variety of multilayers. The model was applied to the characterisation of $La_{0.67}Sr_{0.33}MnO_3\backslash SrTiO_3\backslash Bi_{0.9}La_{0.1}FeO_3$ trilayer films as a function of the different relative layer compositions in these nanostructures.

RESUMO

Os filmes finos multicamada são estruturas compostas por camadas de vários materiais diferentes e são normalmente preparadas para aplicações específicas, pretendidas. A difração de raio-X é uma técnica não destrutiva particularmente adequada para estudar as suas propriedades estruturais. No entanto, extrair parâmetros estruturais da difração de raio-X, como o espaçamento entre planos atómicos individuais, rugosidade entrecamadas ou tensão, requer a modelização e ajuste de espectros de difração de raio-X.

Neste trabalho, apresentamos um modelo cinemático para ajustar os espectros de difração de raio-X medidos em altos ângulos, que inclui tanto a estrutura atómica média das camadas bem como a desordem estrutural. Este modelo permite extrair a composição (espessura das camadas), desordem intra camadas e interfacial, à escala atómica, que é assumida como sendo cumulativa ao longo da multicamada. Para além do modelo cinemático também usamos um modelo ótico aplicado a reflectometria de raios-X (em baixos ângulos) que nos permite obter a composição (espessura e densidade eletrónica das camadas) e rugosidade interfacial. Ao contrário de ajustes mais simples de diffractogramas de raio-X que usam funções como Gaussiana, Lorentziana ou pseudo-Voigt, este modelo permite uma determinação mais completa e precisa dos parâmetros estruturais.

Ajustando os perfis medidos é possível determinar quantitativamente tanto as constantes de rede como os parâmetros de desordem para uma vasta gama de multicamadas. O modelo foi aplicado na caracterização de filmes com tricamadas de $La_{0.67}Sr_{0.33}MnO_3\backslash SrTiO_3\backslash Bi_{0.9}La_{0.1}FeO_3$ em função das diferentes composições relativas das camadas nestas nanoestruturas.

CONTENTS

LIST OF FIGURES

LIST OF TABLES

ACRONYMS

LSMO	$La_{0.67}Sr_{0.33}MnO_3$
STO	$SrTiO_3$
BLFO	$Bi_{0.9}La_{0.1}FeO_3$
BSL	$La_{0.67}Sr_{0.33}MnO_3\backslash SrTiO_3\backslash Bi_{0.9}La_{0.1}FeO_3$
XRD	X-ray diffraction
SAXS	small-angle X-ray scattering
WAXS	wide-angle X-ray scattering
PLD	pulsed laser deposition
PVD	physical vapour deposition

1

INTRODUCTION

Heterostructures can give origin to physical phenomena that would be difficult or even impossible to achieve any other way. Many of these phenomena depend on the structural properties of the multilayers. As such, it is essential to have an accurate structural characterisation of the multilayers. Several techniques allow this type of characterisation, among them the X-ray diffraction (XRD) is well suited for this job. This technique not only provides an accurate structural characterisation of the individual layers at the atomic scale but it is also non-destructive, affordable and readily available.

The technique is important, but we also need a reliable model that describes the data to obtain the structural information. A simple approach is to fit the XRD spectra with Gaussian, Lorentzian, or pseudo-Voigt functions to obtain the lattice parameters, grain size and strain information. However, to get a more detailed characterisation, we need a model that describes the structure. An optical model like the transfer-matrix method that resorts to Fresnel equations allow such characterisation. It takes into account phenomena like the total reflection and surface disorder. This method works particularly well in small-angle X-ray scattering (SAXS) to detect electronic density changes.

On the other hand, wide-angle X-ray scattering (WAXS) is sensible to the atomic spacing and requires a different model. Fullerton et al. [1] and Meng et al. [2] present a kinematic model to describe WAXS of superlattice structures. Their models assume an integer number of atomic planes and are limited to periodic bilayers. However, we want to study non-periodic multilayers. Thus, we developed a kinematic model to accommodate an arbitrary number of non-periodic layers with a real number of planes. We subsequently developed a suitable fitting software to perform the analyses of WAXS diffractograms with that model.

Here, we will describe and apply both models to analyse the structure of multilayer samples. These samples are composed of $La_{0.67}Sr_{0.33}MnO_3\backslash SrTiO_3\backslash Bi_{0.9}La_{0.1}FeO_3$. They combine multiferroic and multilayer properties to produce a spin-filtering effect.

1.1 X-RAY DIFFRACTION

XRD is a nondestructive technique that employs radiation with a wavelength in the order of the interatomic distance and allows the structural characterisation of materials[3]. More specifically it permits the obtention of structural information such as the type and parameters of a crystal lattice, preferred crystallographic orientations, the crystallinity of the material, and information about the crystallites like grain size, strain states, roughness, and several others.

The X-ray radiation interferes with the lattice and is scattered. The interference can be constructive yielding maxima of intensity when the difference between travelled paths is an integer multiple (n) of the incident wavelength λ. For specular reflection of a monochromatic radiation (see fig. 1), the condition for constructive interference is given by Bragg's Law[3]:

$$2d\sin\theta = n\lambda \tag{1}$$

, where d is the distance between diffraction planes in a crystal lattice and θ is the angle of incidence. With specular reflection, the incident and reflected angles are the same, which means the radiation is scattered by an angle of 2θ, known as scattering angle, see fig. 1.

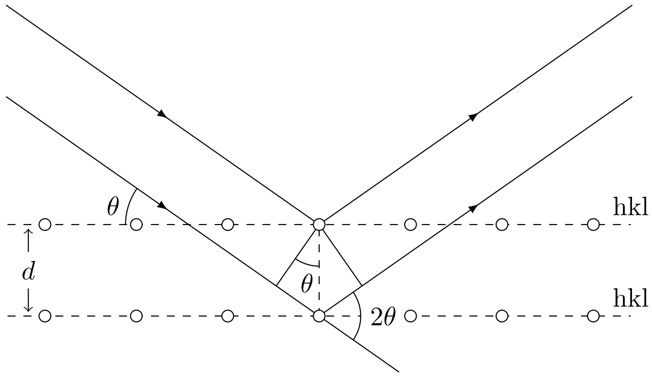

Figure 1: Bragg diffraction of X-ray by a crystal lattice. Two identical X-ray beams are scattered by atoms from a crystal lattice. The scattered beams have a travelled distance difference between them of $2d\sin\theta$. Constructive interference occurs when this difference is equal to an integer multiple of the radiation wavelength.

It's common to separate the XRD is two regions, small (2θ typically below 10°) and wide angle (2θ above 10°)[1], named small-angle X-ray scattering (SAXS) and wide-angle X-ray scattering (WAXS), respectively. The shape of the spectra in those regions is different and requires distinct analyses. The information provided by each region is also different.

SAXS is sensitive to electronic density changes, interfaces and chemical modulation. Optical models provide reasonable descriptions for SAXS. These models can take into account the interfaces and the total reflection phenomenon. With them, we can determine the total thickness, associated with the Kiessig fringes[4], the period of superlattices, associated with the Bragg peaks and the interfacial and interdiffusion roughnesses.

On the other hand, WAXS is sensitive to structural changes, namely changes in the distance between atomic planes, interlayer order, and chemical modulation. Unlike in SAXS, a kinematic model provides a reasonable description for WAXS.

Several techniques allow the structural characterisation of multilayer thin films, each with its advantages and disadvantages. Some benefits of XRD is that it is nondestructive[3]. Air does not absorb much the X-ray, so, a vacuum is not required. Low energy XRD is readily available, can be performed quickly and is relatively inexpensive. Diffraction can be done with the wave-vector in practically any orientation, allowing getting information on different nanostructure directions.

However, XRD also has its disadvantages. It requires a large enough sample and some structural order; therefore, small structures that are present only in trace amounts will often go undetected. In general, the heavier the atom, the stronger the interaction with the X-ray, as such, light elements can be difficult to detect.

1.1.1 θ–2θ METHOD

The X-ray apparatus can use different measurement configurations, the most common is the θ–2θ. In this configuration, the source of X-ray remains fixed, while the sample and detector are rotated by θ and 2θ, respectively. Moreover, the distance between the sample and source, and between the sample and detector remain constant during the measurement[3]. The basic X-ray optics for this type of setup are illustrated schematically fig. 2.

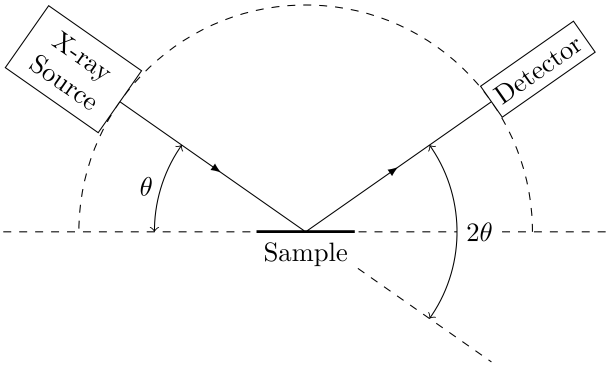

Figure 2: Simplified schematic of an XRD measurement apparatus in a θ–2θ configuration. In this configuration, the sample and detector are rotated by θ and 2θ, respectively.

For an elastic scattering, the incident and scattered waves have the same wavelength, and consequently, the wave vectors have the same magnitude. In the case of specular reflection, both wave vectors make the same angle θ with the surface. The scattering vector, in that case, follows Laue's condition:[5, 6]

$$\vec{q} = \vec{k}' - \vec{k} \tag{2}$$

, where $\vec{k}$ and $\vec{k}'$ are the incident and scattered wave vectors, respectively. In this case, the scattering vector is always perpendicular to the surface[5], see fig. 3. Since the scattering vector is perpendicular to the surface, we scan the structure along the growth direction of the thin film[7].

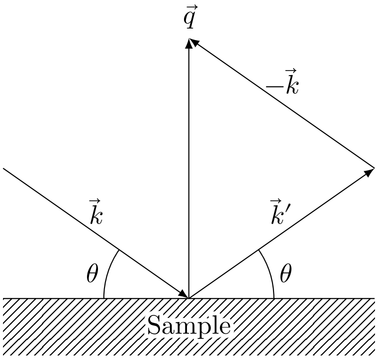

Figure 3: Geometry of the scattering vector construction in an elastic X-ray diffraction. The incident wave vector $\vec{k}$, reflected wave vector $\vec{k}'$ and the scattering vector $\vec{q}=\vec{k}'-\vec{k}$, that satisfies the Laue condition.

1.1.2 RADIATION

To perform XRD we need a source of X-ray radiation, the most common in small laboratories are X-ray tubes with a copper anode. These tubes emit non-monochromatic characteristic radiation with both a continuous spectrum through Bremsstrahlung and discrete emission peaks[3]. The most significant emission lines for copper tubes are the following, in the Siegbahn notation[3, 8–12][1]:

CuKα_1	1.540 59 Å
CuKα_2	1.544 42 Å
CuK$\beta_{1,3}$	1.392 23 Å

It is desirable to have a monochromatic radiation, because it would only produce a single diffraction per family of crystal planes, simplifying the analysis. Therefore, it is necessary to select one peak from the polychromatic radiation emitted by the tube; naturally the most

---

[1] Other X-ray emissions for different elements can be found in the NIST X-Ray Transition Energies Database[13] or the Spectr-W^3 Database on Spectroscopic Properties of Atoms and Ions[14].

intense is chosen. There are two ways to achieve this, with a monochromator or an appropriated filter placed before the detector[3]. With the use of one of them, it is possible to select the CuKα radiation, mitigating the remaining emissions[11].

The CuKα radiation is composed by two peaks, the CuKα_2 having half the intensity of CuKα_1. For simplicity, we will consider the incident radiation is monochromatic, with a wavelength that is the weighted average (CuK$\bar{\alpha}$) of the doublet, with the following wavelength and energy[8, 11]:

CuK$\bar{\alpha}$	1.541 84 Å	8.041 keV

The CuKα X-ray has a typical penetration depth of a few tens of micrometres in solid materials[15], which makes it a natural choice for the structural characterisation of thin films. However, if the thin film thickness is well below the depth penetrated by the X-ray, the signal from the thin films will be obscured by the signal from the substrate. The penetration depth is given by the absorption μ times the sine of the incident angle[15].

$$\tau = \mu \sin(\theta) \tag{3}$$

Note that the depth depends on the sine because the angle is defined between the surface and the incident beam, as shown in fig. 1. Since the depth is proportional to $\sin(\theta)$, it is possible to control the measured depth to a certain extent. The less the substrate is penetrated, the better signal-to-noise ratio of the spectra, meaning that the spectra as less intensity from the substrate obscuring the thin film peaks. The peaks of the spectra present multiple orders at different angles, as such, we can select the lowest possible order that fully penetrates the film to obtain the best signal-to-noise ratio.

The absorption length is defined by Beer-Lambert law as when the beam flux drops to $1/e$ of its incident flux, and is given by:[15, 16]

$$\mu = \frac{\lambda}{4\pi\beta} = \frac{1}{2\lambda r_e \sum\limits_a \rho_a f_{i_a}} \tag{4}$$

, where r_e is the Lorentz classical electron radius (2.818 fm in SI units[16]), $\rho_{j,a}$ the atomic density, f_{i_a} the imaginary atomic scattering factor for each atom of a in the layer j, and β is the imaginary part of the material refraction index. The refraction index will be explored in more detail in section 3.1. Typically, the absorption length has values around 0.1 to 1 mm for β of 10^{-7} to 10^{-8}[16]. The penetration depth is also inversely proportional to the X-ray wavelength, the material's density and absorption.

1.1.3 SPACING FORMULAE

The interplanar spacing d depends on the lattice type. The relation between the unit cell parameters and the spacing for the cubic system is given by:[17]

$$\frac{1}{d^2} = \frac{h^2 + k^2 + l^2}{a^2} \tag{5}$$

, and for the hexagonal is

$$\frac{1}{d^2} = \frac{4}{3}\frac{h^2 + hk + k^2}{a^2} + \frac{l^2}{c^2} \tag{6}$$

Note, that as referred in section 1.2.3, the perovskite derived structures usually are described with a pseudocubic system because they have small deformations when compared with the perfectly cubic perovskite structure.

After determining the spacing of diffraction peaks, we can identify the crystallographic phases by comparing it with known values in the Powder Diffraction Files (PDF) from The International Centre for Diffraction Data (ICDD) powder diffraction database.

1.1.4 MODELS

Each time the incident radiation crosses atomic planes, part of it is transmitted, and another is reflected. The reflected radiation can encounter other planes, and the same effect will happen once again. The reflected radiation during its propagation can interfere with the remaining radiation. The dynamical theory of diffraction describes the effects of these multiple reflections and the interference they give rise[4, 18–20].

Dynamic diffraction is important in perfect crystals but not so much in crystals with imperfections, since the imperfections do not permit a perfect periodicity in the whole crystal[3]. The radiation can be reflected so many times that its mean travelled distance becomes higher than the coherence length. In that case, occurs an extinction of the observed beam at the crystal's exit. In which case, the interference phenomena contribution should not be significant. In those situations, we can use a kinematic approximation. Although an approximation, it has the advantage of being simpler and better suited for the interpretation of the diffraction patterns used for structural determination.

In kinematic models, the scattered intensity maximum is proportional to the square of the number of atomic planes N in the crystal. Thus, the scattered intensity may become unlimitedly large ($I \to \infty$ when $N \to \infty$). By conservation of energy, this can not happen, else, the scattered beam intensity would be greater than the incident. The beam is absorbed as it penetrates the sample, progressively decreasing the effective incident intensity on the more interior planes, and consequently, decreasing the intensity scattered by them. However, the kinematic models assume the scattered photons result only from the collision with collision centres, in the middle of each layer. Thus, the kinematic model assumes the incident beam intensity is the same, independently of the depth of the atomic planes to the sample's surface. This is a limitation of the kinematic models, which makes them only applicable when the interaction of the X-ray beam with the sample is reduced, the number of atomic planes of the structure is small, or the grain size is small, so, that multiple internal reflections can be ignored. Typically, this occurs for nanoscopic materials in measurements done at wide angles, typically scattering angles $2\theta > 10°$.

On the other hand, if the X-ray coherence length is relatively large in relation to the thickness of the sample, then the kinematic theory no longer is applicable. In those cases, it is necessary to resort to the dynamic theory to calculate the scattered intensity. This situation is verified, e.g., in epitaxial films or for X-ray measurements carried out at small angles. Based on the dynamic scattering formulation developed by Darwin[4, 19, 21–23] is possible to construct an optical formalism that permits the development of recursive formulae that are relatively simple to implement in fits of experimental spectra. They are valid provided that the electronic density of the nanostructures can be considered continuous. These theories, allow the modelling of, namely, the refraction phenomena, total reflection and absorption, which are important in the measurement regions of small angles.

1.2 MATERIALS

1.2.1 MULTIFERROIC MAGNETOELECTRIC MATERIALS

Magnetic moment and electric dipole are usually mutually exclusive in crystals[24]. However, multiferroic materials breaks this principle of exclusion. These materials exhibit several ferroic orders simultaneously in the same phase, namely ferromagnetic, ferroelectric or ferroelastic orders[24–31]. As such, multiferroic materials, depending on the ferroic orders they possess, can have properties like magnetoelasticity, magnetoelectricity and piezoelectricity. In fig. 4 we can see the schematisation of the relation between multiferroics as well as the ferroic orders and their properties. The overlap between ferromagnetic and ferroelectric corresponds to multiferroic magnetoelectric materials.

Ferroelectric materials have a spontaneous electric polarisation that is stable and can be reversed by an external electric field and follows a

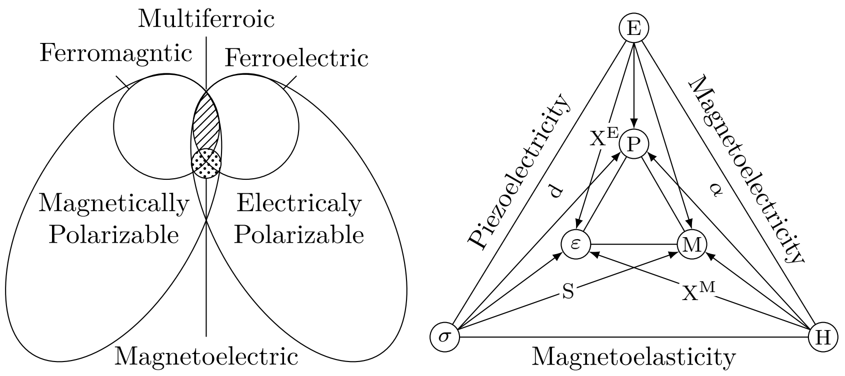

(a) (b)

Figure 4: Relationship between multiferroic and magnetoelectric materials. (a) Venn diagram with the relation between multiferroics and magnetoelectrics, illustrating the requirements to achieve both[32–35]. It should be noted that in this diagram we only consider the type of multiferroics that are simultaneously ferromagnetic and ferroelectric. (b) Schematisation of the possible cross-couplings in multiferroics. Mechanical stress $\vec{\sigma}$, electric field $\vec{E}$ and magnetic field $\vec{H}$, and electric polarisation $\vec{P}$, magnetisation $\vec{M}$ and strain $\vec{\varepsilon}$. There remaining letters represent the different coupling coefficients.[26, 28, 31–33, 35].

hysteresis loop[34], see fig. 5a. Ferromagnetic materials have a spontaneous magnetisation that is stable and can be reversed by an external magnetic field and follows a hysteresis loop[34], see fig. 5b.

Magnetoelectric materials possess a coupling of between their electric and magnetic degrees of freedom. This coupling enables the induction of a magnetisation $\vec{M}$ through the application of an external electric field $\vec{E}$, but also the inverse, the appearance of electric polarisation $\vec{P}$ by applying a magnetic field $\vec{H}$[24, 28, 29, 31, 34, 36, 37]. This effect is observed in some, but not all, multiferroic materials that present simultaneously ferroelectricity and a magnetic order, like ferromagnetism, as schematized by the Venn diagram in fig. 4. These materials follow $\vec{E}$-$\vec{M}$ or $\vec{H}$-$\vec{P}$ hysteresis loops that look somewhat similar to the ferroelectric or ferromagnetic hysteresis loops[38], as seen in fig. 5c. Nevertheless, these properties are neither necessary nor sufficient for magnetoelectricity[39]. Magnetoelectricity is an independent phenomenon from both ferroelectricity and ferromagneticity, but it is typical for this type of materials, emerging either directly or via strain[31, 34], and can only be large in ferroelectric or ferromagnetic materials[36]. The origin of the magnetoelectric coupling can be intrinsic to the material itself, or it can be the result of the combination of the properties of different materials[28].

Magnetoelectric multiferroics with their coupling between ferroelectric and ferromagnetic properties allow a magnetic control of ferroelectric domains or an electric control of magnetic domains, which leads to new possibilities in the design of data storage devices[24, 31, 40–

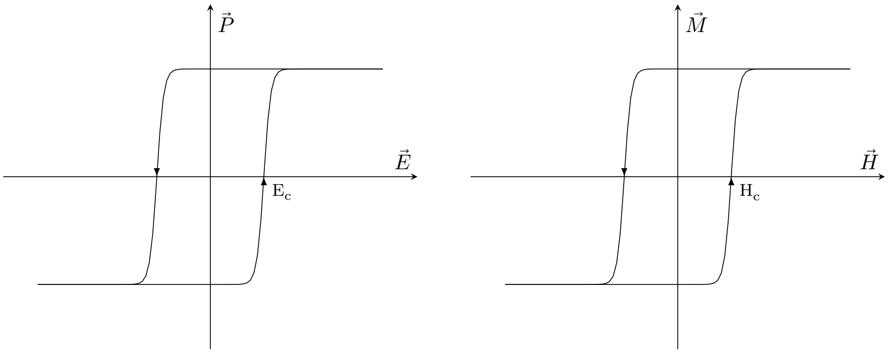

(a) Ferroelectric (b) Ferromagnetic

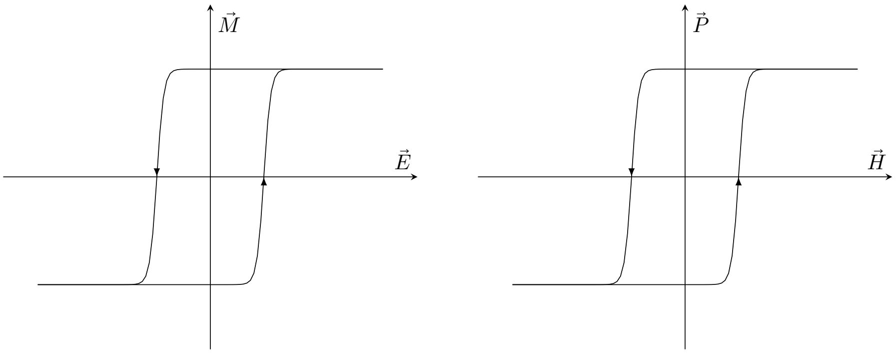

(c) Magnetoelectric

Figure 5: Hysteresis loops typical in ferroelectric, ferromagnetic and magnetoelectric materials. (a) Hysteresis loop of $\vec{P}$ *vs.* $\vec{E}$ typical of a ferroelectric. (b) Hysteresis loop of $\vec{M}$ *vs.* $\vec{H}$ typical of a ferroemagnetic. (c) Hysteresis loops that occur in ferroelectric materials with magnectoelectric properties.[24, 40]

42]. Some multiferroics can be ferroelectric and ferromagnetic, which provides an opportunity to encode information in four logic states, using both electric polarisation and magnetisation[31, 43]. $Bi_{0.9}La_{0.1}FeO_3$ is one of such materials[44].

The transport of information through electron spins, instead of charge, represents an important step to integrate both memory and logic in a single storage device[24, 41, 45, 46]. Spin-filters presents a way to create a spin-polarised electron current. A spin-filter is a device that filters electrons with spin unpolarised that tunnel between two ferromagnetic metallic layers through an insulator barrier. To achieve a spin-filtering effect the insulator acts as a barrier that is higher for a spin direction than the other giving different probabilities to tunnel depending on the electron's spin[47, 48]. Currently, also exists an interest in imaging spin-filter techniques[49]. Multiferroics exhibit electric and magnetic orders simultaneously, making them promising spin-filter materials[43, 49].

1.2.2 PEROVSKITE

Although considerable research has been carried out to find multiferroic materials, only a few single phase materials present both multiferroic and magnetoelectric properties at room temperature[50–52]. Bismuth lanthanum ferrite ($Bi_{0.9}La_{0.1}FeO_3$), commonly referred as BLFO, is one of the most promising magnetoelectric multiferroics at room temperature.

In this work we studied trilayered thin film samples composed of a layer of BLFO followed by strontium titanate $SrTiO_3$ (STO) and lanthanum strontium manganite $La_{0.67}Sr_{0.33}MnO_3$ (LSMO) on top of a STO substrate, has presented on fig. 6.

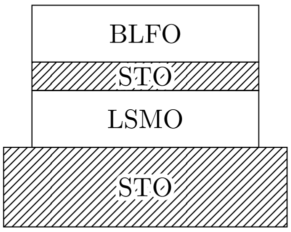

Figure 6: Multilayered structure of the studied thin films.

The STO and LSMO were chosen not only for their properties but also because they share with the $Bi_{0.9}La_{0.1}FeO_3$ (BLFO) the same type of lattice structure and have similar lattice parameters. All the used materials have a perovskite crystalline structure, with chemical formula ABO_3, where A is a divalent or trivalent metal and B is a trivalent or tetravalent metal. This crystalline structure is formed by a cubic lattice of cations A with both a body-centred cation B and face-centred oxygen ions. The unitary cell of the structure is depicted in fig. 7, as well as, the BO_3 octahedron.

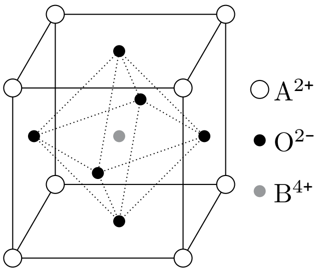

Figure 7: Perovskite's cubic unit cell.

The stability and distortion of the perovskite crystalline structure depend on the ratio of the ionic radii. The Goldschmidt's tolerance factor t[27, 53–56] is a dimensionless number used to describe this, and is given by:

$$t = \frac{r_A + r_O}{\sqrt{2}(r_B + r_O)} \tag{7}$$

, where r_A, r_B, and r_O are respectively the radii of the A, B, and the oxygen ions. A Goldschmidt's tolerance factor of 1 means that the perovskite structure is cubic[54, 57]. The cubic perovskite structure is stable for Goldschmidt's tolerance factors between 0.89 and 1.02[53, 58–60]. When the factor is different, the cell becomes distorted and occurs rotations of the BO_3 octahedron, given rise to non-cubic structures. In table 1, we can see the correspondence between the Goldschmidt's tolerance factor and the type of perovskite crystalline structure. A factor between 0.75 and 1.00 is a necessary condition to form a perovskite, but it is not sufficient[61].

Table 1: Perovskite structure given the Goldschmidt's tolerance factor[53, 58–60].

Goldschmidt's tolerance factor	Perovskites Structure	Explanation
> 1.02	Hexagonal	A-site cations are too large to fit into their interstices
0.89 – 1.02	Cubic	Both A and B-site cations fit exactly into their allotted sites
0.75 – 0.89	Orthorhombic Rhombohedral	A-site cations are too small to fit into their allotted sites
< 0.75	Different structures	Both A-site cations and B-site cations are of same size

The STO has a Goldschmidt's tolerance factor of 1.00[53, 57, 60, 62], giving a cubic perovskite structure. Both the LSMO and BLFO on the other hand present a rhombohedral distortion[7, 44, 63, 64].

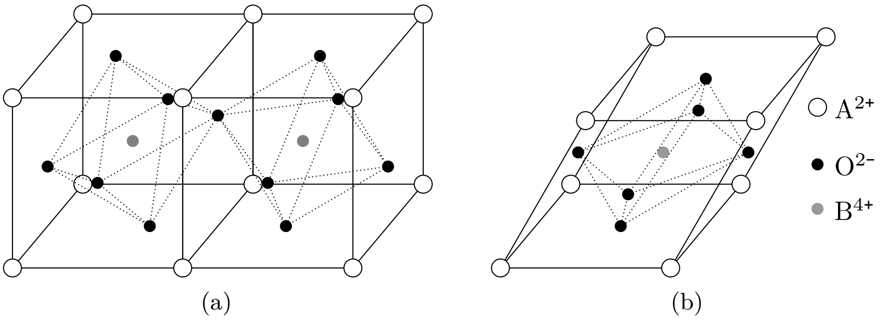

(a) (b)

Figure 8: Common distorted perovskite structures. (a) Orthorhombic. (b) Rhombohedral. $\vec{P}$ is the electric polarization.

Due to changes in the B–O bonds, the octahedron is distorted leading to structural distortions. The displacement of B in the octahedron and rotations of the octahedron, due to variations in the B–O–B angle are also a common cause[65]. In proper multiferroics, the ferroelectricity emerges due to the classical stabilisation of off-centred ions that lead to a macroscopic electric dipole[66]. Most of these compounds crystallise into a perovskite structure[51, 67]. Depending on the combination of the A and B cations, the perovskite can be an insulator, conductor or superconductor. It can present ferroelectric, ferromagnetic or even nonlinear optical behaviours[27].

A distorted perovskite, usually, does not change much from its cubic form, and as such, it is common to describe it using a pseudocubic system instead of a orthorhombic one. The orthorhombic lattice parameter a is related to the pseudocubic parameter a_0 by the relation:

$$a = \sqrt{2}a_0 \tag{8}$$

The relation between both lattices is visible in fig. 9.

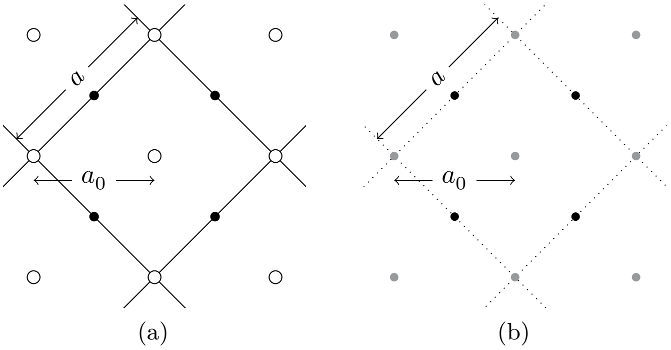

(a) (b)

Figure 9: Relation between orthorhombic and pseudocubic lattices. Orthorhombic lattice viewed along the crystal's c-axis direction, parallel to the diagonals of the perovskite cube, i.e., [001] for the hexagonal system or [111] for the pesudocubic one.

The $La_{0.67}Sr_{0.33}MnO_3$\\$SrTiO_3$\\$Bi_{0.9}La_{0.1}FeO_3$ (BSL) samples are made from perovskites. In this section, we present a brief description of the materials that compose the samples, by deposition order. We will review their structural and electromagnetic characteristics that are essential for the proposed applications and the XRD analysis we will perform.

1.2.3 LANTHANUM STRONTIUM MANGANITE

Lanthanum strontium manganite (LSMO), has the chemical formula $La_{1\text{-}x}Sr_xMnO_3$. Its crystalline structure depends on the doping level x. For x<0.2, the structure is orthorhombic, between 0.2<x<0.5 is rhombohedral and for x>0.5 becomes tetragonal, at room temperature, and monoclinic, at low temperatures (see fig. 10). The samples we studied have a doping level of 0.33, so it has a cubic perovskite structure with a rhombohedral distortion. The colossal magnetoresistive manganites perovskites have small distortions from the cubic structure, therefore, they are usually described according to a pseudocubic notation[7, 63]. At room temperature, the $La_{0.67}Sr_{0.33}MnO_3$ crystal structure has the following parameters: a=5.5023 Å and c=13.3569 Å in the $R\bar{3}c$ space group[68, 69], see table 2.

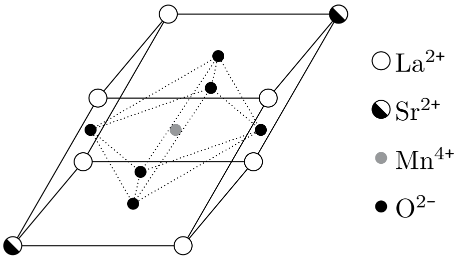

Figure 10: $La_{0.67}Sr_{0.33}MnO_3$ unit cell.

$La_{0.67}Sr_{0.33}MnO_3$ has a Curie temperature T_C around 370 K[69]. Below this temperature, it acts as a conductor to electrons of one spin orientation, but as an insulator or semiconductor for electrons with spins of opposite directions[27, 70]. Also, below T_C, the spins of its electrons are aligned ferromagnetically thanks to the double-exchange interaction caused by doping the $LaMnO_3$ with Sr on the La-site[33].

In the doping range $0.2<x<0.4$, the ground state of the LSMO is ferromagnetic and is one of the perovskite manganites that shows the colossal magnetoresistance effect[63, 71]. The colossal magnetoresistance in this material is a result of the competition between two magnetic interactions, the double exchange and the superexchange[33]. However, the properties of manganite thin film can be different from the bulk materials mainly due to strain[7, 63]. At T_C occurs a phase transition from ferromagnetic to paramagnetic[69, 70]. Thus, at room temperature, it is ferromagnetic.

1.2.4 STRONTIUM TITANATE

Strontium titanate (STO), has the chemical formula $SrTiO_3$. The STO has a cubic perovskite structure (see fig. 11), with a Goldschmidt's tolerance factor of 1.00[53, 57, 60, 62]. At room temperature, the $SrTiO_3$ crystal structure has the following parameters: a = 3.905 Å in the Pm3m space group[60, 72], see table 2.

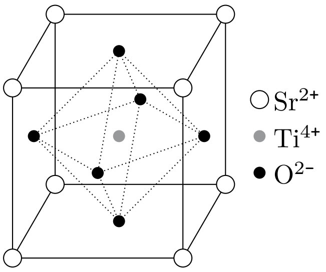

Figure 11: $SrTiO_3$ unit cell.

STO is a good insulator with an indirect band gap of 3.2 eV, at a temperature of 0 K. At room temperature, the STO has a large dielectric permittivity (300)[60].

It is a substrate well suited to grow oriented LSMO films, due to the similarity of its lattice parameters with the pseudocubic ones from LSMO (see table 2) that allow the growth of the films with a small mismatch strain.

1.2.5 BISMUTH LANTHANUM FERRITE

Bismuth lanthanum ferrite (BLFO), is a magnetoelectric multiferroic with the chemical formula $Bi_{1\text{-}x}La_xFeO_3$. The non-doped $BiFeO_3$ at room temperature displays simultaneously large ferroelectric polarisation and weak ferromagnetism, but only in thin film form[51, 52]. Doping the crystal with La atoms to replace Bi atoms induces a “crystal pressure”[73]. A small La doping of x=0.1 stabilises the perovskite phase of the $BiFeO_3$[74]. For this doping level, the BLFO has a pseudocubic perovskite structure with a rhombohedral phase, see fig. 12. At room temperature, the $Bi_{0.9}La_{0.1}FeO_3$ crystal structure has the lattice parameters present in table 2.

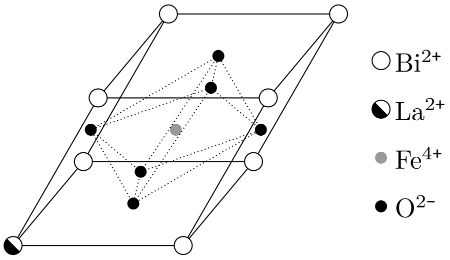

Figure 12: $Bi_{0.9}La_{0.1}FeO_3$ unit cell.

The “crystal pressure” induced by the La doping can transform the crystal’s structure from a rhombohedric phase into orthorhombic, see fig. 8[73]. Nevertheless, for a doping of x=0.1, the pressure is not high enough, and the structure remains rhombohedric. The $BiFeO_3$ suffers from leakage currents, but the La doping also allows a reduction of the current density in six orders of magnitude. The BLFO remains ferromagnetic at room temperature for x<0.3, losing it at higher temperatures[44].

Now that we discussed the structural and electromagnetic properties of the used materials, we present in table 2 a resume of their structural information that is relevant for the XRD analysis. In this table, we display the hexagonal lattice parameters, a and c, for the rhombohedric materials and their approximated pseudocubic, a_0. From the pseudocubic lattice constants, we used Bragg’s Law from eq. (1) to estimate the scattering angles 2θ for the (100) planes, taking into account the conditions used for the XRD measurements.

Table 2: Summary of the structural information of the used materials. The lattice parameters a and c are in the hexagonal system, and the a_0 in the pseudocubic system. Using Bragg's Law and the pseudocubic lattice parameters we estimated the scattering angles 2θ for the (100) planes.

Material	Lattice	a(Å)	c(Å)	a_0(Å)	$2\theta_{100}$(degree)
LSMO[68, 69]	Rhombo.	5.502	13.357	3.891	22.856
STO[60, 72]	Cubic	—	—	3.905	22.772
BLFO[44]	Rhombo.	5.578	13.806	3.944	22.544

2

EXPERIMENT

In this work, we studied multilayered thin films. These samples consist of three layers of perovskites with a few nanometers each consecutively deposited on top of a substrate. Exists a diverse multitude of techniques that allow the production of such samples. A subset of those techniques are the physical vapour deposition (PVD), that consists of the physical release of material from a target and its transport to a substrate. The studied samples were produced with a technique called pulsed laser deposition (PLD) that belongs to this group.

2.1 PULSED LASER DEPOSITION

PLD is a conceptually simple technique that uses a high power pulsed laser to eject material from a target. Figure 13 depicts a schematic diagram of its basic setup.

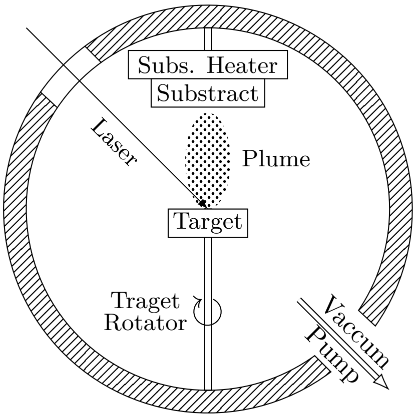

Figure 13: Schematic of a pulsed laser deposition system. A pulsed laser impinges on a target, removing material that deposits on a substrate, forming a thin film on its surface.

The deposition is effectuated inside a vacuum chamber that, if required, can be filled with a background gas. Inside are several targets that are individually illuminated by a pulsed laser. The absorbed electromagnetic energy is converted into electronic excitation that converts into thermal energy, leading to melting and vaporisation of the target. The ejected material forms a plasma plume, made by energetic neutral and ionic species, including polyatomic species[33]. The plume expands perpendicular to the target surface, depositing on a substrate, forming a thin film. The process is then repeated until the layer has the required thickness, afterwards, each the target is changed to create the next layer, repeating the procedure till the samples have all the desired layers.

Now, we show a more in-depth review of the PVD process, which comprises three major steps that are be repeated several times during a deposition, they are[75, 76]:

1. Vaporisation of the target material
2. Transport of the formed vapour plume
3. Growth of a thin film on the substrate surface

2.1.1 TARGET ABLATION

The first step in the procedure is the extraction of the material that will be deposited. For that, a target is irradiated by a pulsed laser, leading to its melting and vaporisation. Figure 14 depicts the essentials of laser ablation[77].

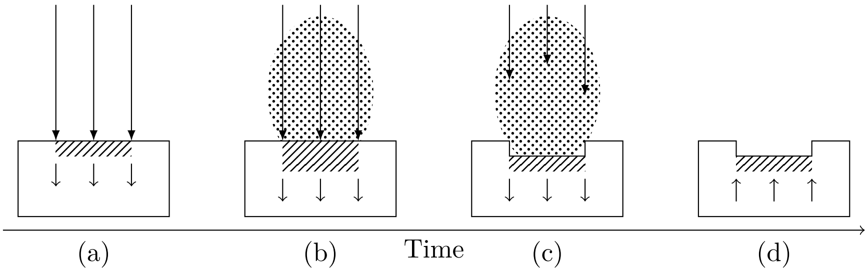

Figure 14: Main steps of pulsed laser ablation. (a) Initial absorption of the radiation (long arrows) and target melting (shaded area, short arrows indicate the motion of solid-liquid interface). (b) Heat flow spreads through the target, leading to its vaporisation and formation of a plume. (c) Vaporisation continuous and the radiation interacts with the plume, prompting the formation of a plasma. (d) Target cooling and solidification.[77]

During the whole process, a pulsed laser beam irradiates a target formed of the desired deposition material, or by a material that will later interact with a background gas to form the desired material. The laser pulse heats the surface, leading to the melting and vaporisation of the target. The ablation occurs due to subsurface heating induced either by the pulse or by the recoil pressure exerted by the material ablated in the initial part of the pulse[76]. As the vaporisation sets in, the latent heat acts as a cooling mechanism that leads the target's subsurface to reach a higher temperature than the surface. Eventually, the continuous subsurface heating provokes an explosion of solid material on the surface, creating a highly forward-directed plasma plume[76, 78]. The pulse eventually ends and, with it, the target heating, prompting the solidification of the material and recession of the melt front.

2.1.2 VAPOUR PLUME TRANSPORT

Heating the target prompts the formation of a plume formed by ejected ions from all of the target elements, that roughly retains its stoichiometry[33]. The plume of ejecta is promptly irradiated by the laser pulse, absorbing radiation in the region where the density of charged particles is higher, that is, within a short distance from the bulk target[79]. This absorption leads to the excitation and ionisation of species in the plume. Furthermore, it simultaneously reduces the intensity of the radiation reaching the target[77]. The plume initially propagates one-dimensionally [76, 77, 80, 81], however, beyond a distance comparable to the dimensions of the laser spot becomes three-dimensional through adiabatic expansion due to the collision of the ejecta with the background gas and with itself, inside the plume[76]. The presence of a background gas slows and eventually stops the plume propagation after a few microseconds[82, 83].

2.1.3 THIN FILM GROWTH

In the final stage, the plume particles arrive and diffuse on the substrate, resulting in the creation of chemical bonds and growth of a thin film on its surface[84]. The morphology of the resulting film depends on several factors, namely, the kinetic energy of the arriving particles, the substrate temperature, the sticking probability, and the deposition rate[85]. Films deposited on substrates at room temperature are usually amorphous. However, their crystallinity can be improved if the substrate is at a higher temperature[77]. High substrate temperatures and low deposition rates facilitate epitaxy, allowing for the diffusion of the adatoms on the substrate until they find equilibrium lattice sites[85]. As such, thin films deposited at low temperatures or high deposition rates tend to become amorphous. Another important aspect of the quality of the resulting thin film is the lattice mismatch between the substrate and the thin film. The properties and quality of the resulting film depend on several deposition factors, such as the choice of substrate and its temperature, the laser wavelength, pulse duration and intensity, and presence or not of background gas[7, 77].

2.1.4 ADVANTAGES AND DISADVANTAGES

Practically any material can be deposited by PVD[77]. Abundant reports have been made on the deposition of diverse materials, including multiferroics[77, 79, 83, 86–93]. It is a cost-effective preparation process that permits, for example, rapid prototyping for a wide range of materials[33]. Furthermore, the deposition can create high-quality epitaxial films due to the high kinetic energy of the plume particles[94]. The congruent transfer of the bulk target material onto the film permits the preservation of its stoichiometry[33, 77, 87].

In addition to the high-quality samples produced by the technique, its implementation also presents advantages in relation to other deposition techniques. PVD does not require ultra-high vacuum[87] and the power source is outside of the chamber. Furthermore, the deposition of multilayers becomes straightforward with the use of multiple targets. The thickness of the layers can be controlled by tuning the material flux, the number of laser pulses or the deposition time. The thickness of the deposited layer is then given by:

$$thickness = f \times t_{dep} \tag{9}$$

, where f is the laser's pulse frequency and t_{dep} is the deposition time.

Nevertheless, it also has disadvantages in relation to other PVD techniques, primarily two are of note. The first relates to the fact that due to the high directionality of the plume, the deposition of large homogeneous films is hindered. The other is the possibility of exhibiting particles (droplets), due to explosive boiling of the target surface, with diameters in the order of the micrometre, which can meaningly affect the film properties[33]. Both of these makes the technique undesirable for industrial applications[28, 33]. However, their presence can be minimized by using lower wavelengths and lower fluences to reduce the possibility of explosive boiling.

2.1.5 LATTICE MISMATCH

The interface between adjacent layers with different structures can present lattice mismatch. This mismatch induces stress in lattices of those layers, which influences their physical properties, e.g., transport and magnetic[33, 55, 95, 96]. The lattice mismatch between a layer i and it neighbouring layer j is defined as[27, 33]:

$$\delta = \frac{2(a_i - a_j)}{a_i + a_j} \approx \frac{a_i - a_j}{a_j} \tag{10}$$

, where a_i and a_j are layers in-plane lattice parameters. Positive δ values indicate tensile (compressive) stress, whereas negative values produce compressive (tensile) stress in-plane (out-of-plane)[27], as schematized in fig. 15. Epitaxial growth typically requires $\delta<0.1$[33]. This should not be a problem in the samples we will analyse as their materials have very close lattice constants and should produce δ well below 0.1. Although the lattice is deformed, the volume of its unit cell is maintained, as such, the tensile stress increases the lattice parameter perpendicular to the surface and decreases the in-plane lattice parameter, compressive stress has the opposite effect.

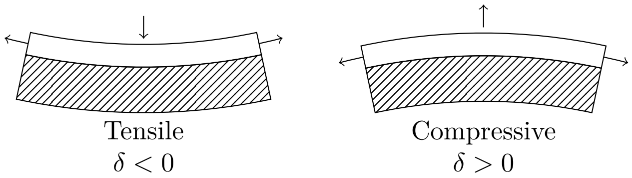

Figure 15: Effects of lattice mismatch on the stress states of thin films.

2.1.6 DEPOSITION SETUP

The PLD depositions were carried out in the pulsed laser deposition facilities of Centro de Física of Universidade do Minho (Gualtar).

Substrates of STO were placed inside a high vacuum chamber, on a resistive heater plate. The heater temperature T_{sub} was measured with a thermocouple placed behind the plate and controlled by a Eurotherm 2116 PID Temperature Controller.

The substrate holder allows movement in a direction perpendicular to the target. With this, it is possible to adjust the distance between the target and the substrate $d_{tar\text{-}sub}$. A target is placed in the centre of the vacuum chamber. During the deposition, the target rotates to allow a more uniform ablation. This, not only allows a higher utilisation of the target materials but it also helps preserve the stoichiometry of the growing film[33]. A multitarget holder enables the deposition of multiple layers in the same deposition run by holding up to 4 interchangeable targets.

Two pumps were used to achieve a high vacuum. An Alcatel Pascal 2010 I rotary pump allows a primary vacuum of 2×10^{-3} mbar. After that, an Alcatel ADP80 turbomolecular pump brings the pressure P_{base} down to the desired 3×10^{-5} mbar.

The chamber was filled with oxygen. This active gas will permit the formation of the oxides. With the introduction of oxygen, the pressure climbs to 0.8 mbar. A needle valve controlled the oxygen flux. While in a rough vacuum, the oxygen pressure was measured with an AML PGC1 Pirani gauge and with a KS 943 cold cathode Penning gauge during high vacuum.

The ablation of the target was carried out with a Lambda Physik® LPXpro™ 210 pulsed excimer KrF laser with a wavelength of 248 nm and a pulse duration of 25 ns. Each pulse carried an energy E_{laser} of either 250 mJ or 450 mJ, depending on the sample. For each material, a pulse frequency f was set. The laser beam irradiates the target at an angle of 45° with its surface.

The described procedure has carried out to produce five multilayered thin film samples with the structure illustrated in fig. 6. A summary of the deposition parameters for the different samples is displayed in the table 3, on the next page. The table 3 also has the expected thickness of each layer. The expected thicknesses were obtained empirically. We assumed a linear deposition rate and calibrated the deposition rates for samples previously produced with the thickness measured. The deposition rates for the used materials and deposition setup are the following:

LSMO	$1/9\,\mathrm{nm\,min^{-1}\,Hz^{-1}}$
STO	$1/2\,\mathrm{nm\,min^{-1}\,Hz^{-1}}$
BLFO	$1/3\,\mathrm{nm\,min^{-1}\,Hz^{-1}}$

2.2 X-RAY MEASUREMENT SETUP

The XRD measurements were carried out at Universidade do Minho (Gualtar). A θ–2θ geometry configuration has used for the XRD measurements. A copper tube was used, as the source of X-ray. With a monochromator we selected the CuKα emissions, giving an incident radiation approximately monochromatic with a wavelength of 1.540 59 Å. A scintillation detector was used to give a count of the diffracted radiation.

Table 3: Summary of the deposition parameters used to produce the studied BSL samples.

Sample	Layer	E_{laser} (mJ)	Beamsplitter	P_{base} (10^{-5} mbar)	Gas	P_{dep} (mbar)	T_{sub} (°C)	$d_{tar\text{-}sub}$ (cm)	f (Hz)	t_{dep} (min)	thickness (nm)
BSL 5	LSMO	450	50%	3.00	O_2	0.8	700	5	3	30	10
	STO	450	50%	3.00	O_2	0.8	720	5	5	2.191	5
	BLFO	450	50%	3.00	O_2	0.8	700	5	3	5	5
BSL 8	LSMO	450/250[1]	50%/99%[1]	3.00	O_2	0.8	700	5.5	6	30/30[1]	20
	STO	450/250[1]	50%/99%[1]	3.00	O_2	0.8	720	5.5	5	1/2[1]	5
	BLFO	250	50%/99%[1]	3.00	O_2	0.8	700	5.5	6	40	80
BSL 9	LSMO	250	99%	3.00	O_2	0.8	700	5.5	6	30	20
	STO	250	99%	3.00	O_2	0.8	720	5.5	5	3	7.5
	BLFO	250	99%	3.00	O_2	0.8	700	5.5	6	10	20
BSL 10	LSMO	250	99%	3.00	O_2	0.8	700	5.5	6	30	20
	STO	250	99%	3.00	O_2	0.8	720	5.5	5	6	15
	BLFO	250	99%	3.00	O_2	0.8	700	5.5	6	20	40
BSL 11	LSMO	250	99%	3.00	O_2	0.8	700	5.5	6	30	20
	STO	250	99%	3.00	O_2	0.8	720	5.5	5	9	22.5
	BLFO	250	99%	3.00	O_2	0.8	700	5.5	6	20	40

[1] half the deposition has carried out with the first values and the second half with later values.

3

SMALL-ANGLE X-RAY MODEL

The small-angle X-ray scattering (SAXS) is a useful XRD technique to study the structure of thin films and multilayered samples. It is particularly helpful to determine structural information, namely the thickness of individual layers, the spacing between diffraction planes and the roughness, of interfaces and surfaces[16, 21, 97].

This type of XRD measurement deals with small angles, typically with scattering angles 2θ below 10°[1]. Kinematic models are not well suited to describe such small angles, for instance, they do not predict total reflection, *etc.* Optical models are more appropriate for this task. These models assume the samples are composed of media with continuous electronic densities and calculate the reflection and refraction at each interface. These media are described by refractive indices, and the knowledge of these is enough to predict what happens at the interfaces[1, 16].

In this chapter, we present a general optical formalism to calculate the reflectivity of rough surfaces and interfaces of multilayers in function of the radiation's incident angle θ, which is valid for SAXS. The formulation will be based on the multilayer structure schematized in fig. 16.

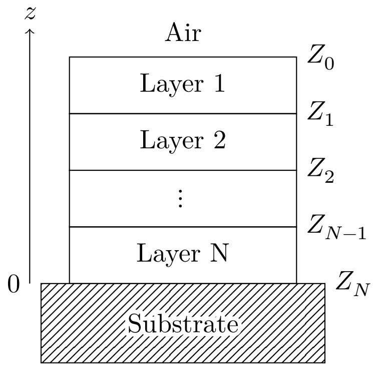

Figure 16: Schematics of the plane of incidence in a stratified medium that will be described by the SAXS model. The system is composed of N+2 layers. Air is labelled layer 0, and layers of the stratified medium have labels $1 \leq j \leq N$. We will measure the travelled distance z from the substrate interface.

This multilayered system is composed of N+2 layers with indices j, each layer is treated as a continuous medium with refraction index n_j. If the penetration depth is smaller than the thickness of the sample, we will deal with N+1 interfaces that separate pairs of adjacent layers with distinct refractive indices. The depth Z_j marks the interface the layers j and $j+1$. The layer with index 0 corresponds to the incident propagation medium, usually air, and the layer N+1 is the substrate. We presume the penetration depth is smaller than the thickness of the sample including the substrate, and as such, we will not consider the reflection that could occur in the interface Substrate/Air.

3.1 REFRACTION INDEX

Photoabsorption and coherent scattering are the two primary interactions with matter in low energy XRD. These processes are accurately described by the complex atomic scattering factor, f=f_r+if_i. The atomic scattering factor is a measure of the scattering amplitude of a wave by an atom. This factor needs to be multiplied by the scattering amplitude of a single free electron to yield the total amplitude coherently scattered of an atom[98].

For photon energies above 50 eV, we can accurately describe the interaction with the X-ray if we consider the crystal as a collection of independent atoms. We will deal with CuK$\bar{\alpha}$ radiation with 8.041 keV, so, well within this regime. Thus, the total scattered amplitude is the sum of the amplitudes scattered by the individual atoms[98].

The interaction of X-ray with matter can be described by optical constants like the complex refraction index. This index is important for a quantitative understanding of the interaction between the X-ray and the materials. Each layer of the multilayer system is characterised by a complex refraction index n_j, in general, the refraction index of matter for X-ray radiation is given by:[6, 16, 97, 98]

$$n_j = 1 - \delta_j - i\beta_j \tag{11}$$

, where the real and imaginary components, δ and β, describe the dispersive and absorptive aspects of the wave-matter interaction. These two parameters depend on the type of radiation. The classical model of an elastically bound electron yields these parameters for the X-ray radiation,[6, 16, 97, 98]

$$n_j = 1 - \frac{\lambda^2 r_e}{2\pi} \sum_a \rho_{j,a} f_{j,a} \tag{12}$$

, where r_e is the Lorentz classical electron radius with 2.818 fm[16], λ the incident radiation wavelength, $\rho_{j,a}$ the atomic density (either in unit cells or atoms per volume unit) and $f_{j,a}$ the complex atomic scattering factor for each atom of type a in the layer j. Photoabsorption determines the atomic form factor as a function of energy, a list of these values can be found in tables, like the ones given by Henke et al. [98]. The α and β coefficients are defined as:[98]

$$\alpha = \frac{\lambda^2 r_e}{2\pi} \sum_a \rho_{j,a} f_{r_{j,a}} \tag{13}$$

$$\beta = \frac{\lambda^2 r_e}{2\pi} \sum_a \rho_{j,a} f_{i_{j,a}} \tag{14}$$

, where the difference is that the α depends on the real part of the atomic form factor and β depends on the imaginary part. The real component can also be defined as:[16]

$$\delta_j = \frac{\lambda^2 r_e}{2\pi} \rho_{e,j} \tag{15}$$

, where $\rho_{e,j}$ is the electronic density of layer j. Which means, that for a fixed wavelength, the refraction index's real part is proportional to the materials electronic density.

3.2 TOTAL EXTERNAL REFLECTION

Since the refraction index in the X-ray is slightly less than 1, the incident radiation impinged on a flat surface can suffer total external reflection[16]. Total external reflection is observed when the incident radiation is below a certain angle, that we will call critical angle θ_c. The critical angle determined by the Snell–Descartes' Law for radiation that comes from a medium with refraction index close to 1, like air, is given by[1]:[16, 99]

$$\cos\theta_c = n_j = 1 - \delta_j \tag{16}$$

For the typical X-ray wavelengths, δ is small enough that we can safely use the small angle approximation for the cosine ($\cos\theta \approx 1 - \theta^2/2$), with it, the critical angle can be approximated to:[16, 21, 99]

$$\theta_c \approx \sqrt{2\delta_j} \tag{17}$$

We rewrite it using eqs. (12) and (15), showing it proportionality to the materials electronic density,

$$\theta_c \approx \lambda \sqrt{\frac{r_e \sum\limits_a \rho_{j,a} f_{j,a}}{\pi}} = \lambda \sqrt{\frac{r_e \rho_{e,j}}{\pi}} \tag{18}$$

As can be seen in fig. 17, because the X-ray is totally reflected, we observe a plateau of maximum reflectivity for angles below θ_c. Total external reflection in X-ray, is observed at incident angles with typical values 2θ<1.0°.

---

[1] Note that eq. (16) is presented with cosine because the angle is defined between the surface and the incident beam, as defined in fig. 1.

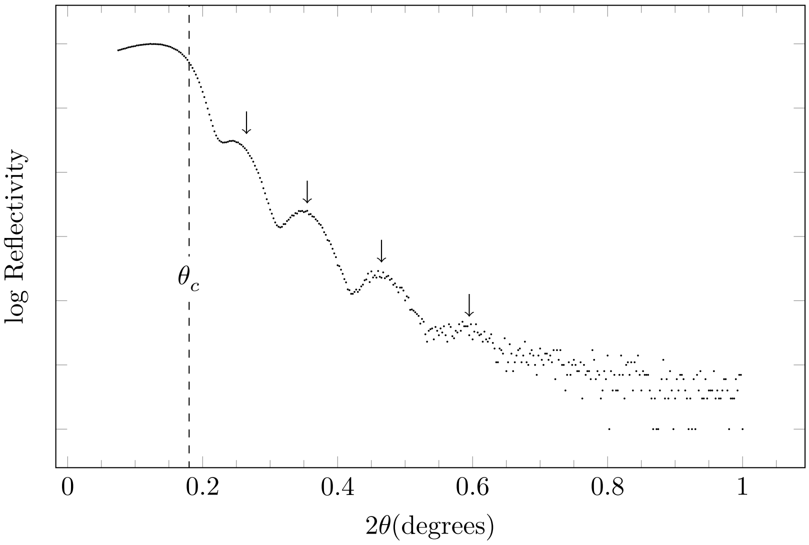

Figure 17: SAXS reflectivity spectra of a single thin film layered sample of $GdMnO_3/MgO$. The dashed line marks the critical angle θ_c, and the vertical arrows indicate the Kiessig fringes.

The X-ray beam is fully reflected from the surface below the critical angle. However, an evanescent wave penetrates a short distance of the thin film. X-ray techniques like the grazing-incidence small-angle X-ray scattering (GISAXS) can exploit this evanescent wave to probe the thin film surface.

3.3 X-RAY REFLECTIVITY IN MULTILAYERS

The SAXS spectra are characterised by a rapid decrease of the reflectivity for angles above the critical angle. This decreasing reflectivity can be modulated by an oscillatory behaviour that produces fringes called Kiessig fringes. Figure 17 gives an example of a SAXS spectrum that displays this type of behaviour. These modulations occur in multilayered systems with layers that have a finite thickness in the order of magnitude of the incident radiation wavelength. In those cases, the radiation will undergo multiple internal reflections that interfere between themselves, given rise to the observed fringes[16, 21]. The angular spacing between Kiessig fringes is inversely proportional to the total film thickness[16]. Due to the relation between these fringes and the layers thicknesses, the roughness in the interfaces surfaces will destroy the coherence and reduce, or even eliminate the fringes. So, well-defined and visible fringes are an indication of a film with sharp interfaces[100].

The radiation is reflected and transmitted on each interface between layers of different refraction indices, and consequently different electronic densities. To describe the reflectivity and transmissivity in a multilayer system we need to take into account the multiple internal reflections that happen. Abeles' matrix method provides a way to describe propagation of radiation through different stratified media. In this approach, the refraction matrix R_j describes the refraction between two media, and is defined as:[16, 101]

$$R_j = \begin{bmatrix} p_j & m_j \\ m_j & p_j \end{bmatrix} \tag{19}$$

, with coefficients p_j and m_j that characterise the relation between the magnitude of the electric fields in the media j and $j+1$, they are defined as:[16]

$$p_j = \frac{k_{j,z} + k_{j+1,z}}{2k_{j,z}} \tag{20}$$

$$m_j = \frac{k_{j,z} - k_{j+1,z}}{2k_{j,z}} \tag{21}$$

The wave vector k_j is defined as shown in fig. 18.

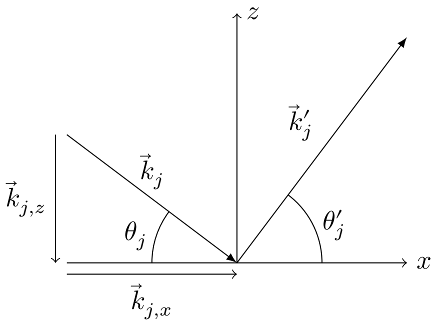

Figure 18: Wave vectors of the incident $\vec{k}_j$ and diffracted $\vec{k}'_j$ waves in a layer j. They are polarised along the y-axis and travel in the xOz plane of incidence.

The components of the wave vector of the incident wave are:

$$k_{j,x} = k_j \cos\theta_j \tag{22}$$

$$k_{j,z} = -k_j \sin\theta_j = -\sqrt{k_j^2 - k_{j,x}^2} = -\sqrt{k_j^2 - k_j^2\cos^2\theta_j} \tag{23}$$

Using the dependence between the wavenumber and the refraction index, we can rewrite the normal component.

$$k_{j,z} = -\frac{2\pi}{\lambda} n_j \sqrt{1 - \cos^2\theta_j} \tag{24}$$

SAXS deals with small angles, as such, we can use the small angle approximation for the cosine.

$$k_{j,z} \approx -\frac{2\pi}{\lambda} n_j \sqrt{\theta_j^2 - \frac{\theta_j^4}{4}} \tag{25}$$

The angles are small enough that the θ_j^2 will dominate the term $\theta_j^4/4$.

$$k_{j,z} \approx -\frac{2\pi}{\lambda}\theta_j n_j \tag{26}$$

, replacing the refraction index, defined in eq. (12),

$$k_{j,z} = -\frac{2\pi}{\lambda}\theta_j\left[1 - \frac{\lambda^2 r_e}{2\pi}\sum_a \rho_{j,a} f_{j,a}\right] \tag{27}$$

$$= \left[\lambda r_e \sum_a \rho_{j,a} f_{j,a} - \frac{2\pi}{\lambda}\right]\theta_j \tag{28}$$

The electric field amplitude oscillates periodically along the radiation travel, possessing a dependence with the travelled time. The translation matrix T_j describes this dependence, and is defined as:

$$T_j = \begin{bmatrix} e^{-ik_j t_j} & 0 \\ 0 & e^{+ik_j t} \end{bmatrix} \tag{29}$$

, where t_j is the thickness of the layer j, and is defined as:

$$t_j = Z_j - Z_{j-1} \tag{30}$$

, where Z_j is the position of the interface between the layers j and j+1, as displayed in fig. 16.

The product of all the refraction and translation matrices of the entire system is the transfer matrix M,

$$M = \left[\prod_{j=0}^{N-1} R_j T_j\right] R_N \tag{31}$$

The reflection coefficient r is the ratio between the reflected and incident electric fields on an interface. Although the X-rays penetration depends on the type of material, it is typically in the order of the micrometer[3, 15, 16], see section 1.1.2, well below the thickness of the typical substrates. Therefore, we assume there is no reflection back from the substrate. In that case, the reflection coefficient is:[16]

$$r = \frac{M_{12}}{M_{22}} \tag{32}$$

In a SAXS experiment we measure the Fresnel reflectivity,

$$R = |r|^2 \tag{33}$$

, which is a real number, unlike the complex reflection coefficient. The reflectivity loses the phase information given by the reflection coefficient.

3.4 ROUGHNESS

Generally, interfaces are not perfect, they have a certain roughness and thickness. The roughness of the top layer is of particular importance to describe how fast the exponential decay above the critical angle occurs. To take into account the reduction in reflectivity caused by the interface roughness, the reflection coefficients from eq. (32) can be multiplied by the Debye-Waller-type factor S_j, defined as:[16]

$$S_j = \frac{r_j^{rough}}{r_j^{flat}} = e^{-q_j^2 \sigma_{j+1}^2/2} \tag{34}$$

, where σ_j^2 is the mean square height on the interface roughness, and q_j it the scattering vector on layer j. The scattering vector in a layer is given by:

$$q_j = \frac{4\pi n_j}{\lambda} sin(\theta) \tag{35}$$

, with refraction index n_j of that layer. We should note that the SAXS spectra are sensitive to the dimension of the overall roughness, independent of its nature[1].

For a multilayer with imperfect interfaces or surfaces, the experimentally measured reflectivity can be fitted by the eq. (33), with the reflection coefficient for that structure determined by eq. (32) and adjusted by eq. (35) to take into account interface roughness. To perform the fitting, we can resort to an optimisation algorithm like the Levenberg-Marquardt algorithm[102, 103].

In summary, for a SAXS reflectivity spectrum, the presented model obtained with the Abeles' matrix method allows the determination of the density and thickness of each layer and the mean height of the interfaces. The critical angle is related to the density of the constituent materials. The reflectivity is modulated, producing fringes. The amplitude of these fringes depends on the roughness of the layers, interface quality and density variations. Furthermore, the separation between fringes is inversely related to the layer thickness[15].

3.5 FITTING

In this section, we will use the former model to analyse the SAXS spectra of our BSL samples. For that, we resorted to the aid of the solver *SimulReflec 1.75*[104] that implements the described model.

To determine the normal component of the wave vector, we need to know the density and atomic form factor of the materials that constitute the sample. We will start by determining the atomic form factors.

The atomic form factor depends on the incident energy and scattering angle. However, it is independent of the scattering angle if the wavelengths are long compared to the atomic dimension (which they are not) or for small scattering angles[98]. Thus, we will consider the atomic form factor are constant in our analysis of the SAXS spectra. The XRD measurements were carried out with a copper tube source that emits radiation with a wavelength of 1.5406 Å, that we will consider as monochromatic for the fits. This wavelength has a corresponding energy of 8047.8 eV, obtained by the Planck-Einstein relation,

$$E = \frac{hc}{\lambda} \tag{36}$$

, for a value of hc of 1.2398×10^5 eV Å^{-1}[105]. Henke et al. [98] provides tables of atomic form factors for a vast selection of atoms and energies obtained through photoabsorption. However, this list does not contain the values for the energy we are dealing. Therefore, we did a linear interpolation using the two closest energies provided to obtain the desired values for our incident energy. The obtained values are presented in table 4. We calculated the form factors for the materials involved: LSMO, STO and BLFO. To do this, we calculated the values for the average unit cells of these materials, and the determined values are displayed in the same table 4.

Table 4: Complex atomic form factor values of the atoms and materials used in the BSL samples.

Atom	f_r	f_i
La	55.6747	9.7817
Sr	37.6425	1.8479
Mn	24.4563	2.8363
O	8.0524	0.0338
Ti	22.2421	1.8711
Bi	79.3175	9.3118
Fe	24.8476	3.2131
LSMO	98.3376	10.1012
STO	84.0418	3.8204
BLFO	125.9580	12.6733

As seen in section 1.2.2, STO presents an almost perfect cubic perovskite lattice. On the other hand, the LSMO and BLFO have rhombohedric perovskite lattices. These rhombohedric perovskites usually have a small deviation from the perfect cubic perovskite, and as such, are treated as pseudocubic[7, 63]. Taking into account this, we used the pseudocubic approximation for those two materials. Thus, we determined the unit cell volume as if it were cubic with the lattice parameters in table 2. Those values were used to determine the atomic density of the used materials, displayed in table 5, that is given by the number of unit cells per volume unit.

Table 5: Lattice parameters a_c and atomic densities ρ of the material used in the BSL samples, in the pseudocubic system.

Material	a_c(Å)	ρ(nm^{-3})
LSMO[68, 69]	3.8907	16.979
STO[60, 72]	3.9051	16.792
BLFO[44]	3.9440	16.300

Now, we need the thickness of each layer to obtain the translation matrix. We started with the expected empirical values for the deposition conditions, which are present in table 3.

Lastly, we need the average height of the interfaces to find the roughness. However, it is hard to know these values a priori, and as such, we resorted to trial and error to get the values that best describe the measured diffraction spectra.

Figure 19 (on pages 34 and 35) displays the SAXS measured spectra for the BSL samples with their respective fits.

A comparison of the spectra in the critical angle region can be seen in fig. 20 (on page 36). We can see that the critical angle varies considerably between samples. The critical angle depends on the electronic density[6, 16], as seen in eqs. (17) and (18). So, it is to expect that samples have different densities, even though they are composed of the same materials.

The spectra of the BSL 5, 8 and 10 samples have more discernible Kiessig fringes than the other two samples. The remaining samples also present fringes, but they have a low amplitude, probably because the interfaces have high roughness. Without well-defined pronounced fringes, the fit procedure is more complicated. As seen from fig. 19, the fits for the BSL 9 and 11 samples do not represent well the spectra, unlike the other three samples.

The substrates were fabricated with high structural quality, and for this reason, we do not expect their structure to deviate much from the literature, see section 1.2.4. As seen in section 1.1.2, the X-ray penetration for the used CuKα in the order of the micrometres and is directly proportional to the angle, as such, it should be orders of magnitude lower than the thickness of the samples. Thus, we do not expect to occur reflection on the interface substrate/air. As such, we will consider the substrate to have a semi-infinite thickness for the fits. Concerning the air, we also considered its layer to have a semi-infinite thickness.

We also considered the atomic form factors to be constant in all layers and given by the values determined a priori presented in table 4. As

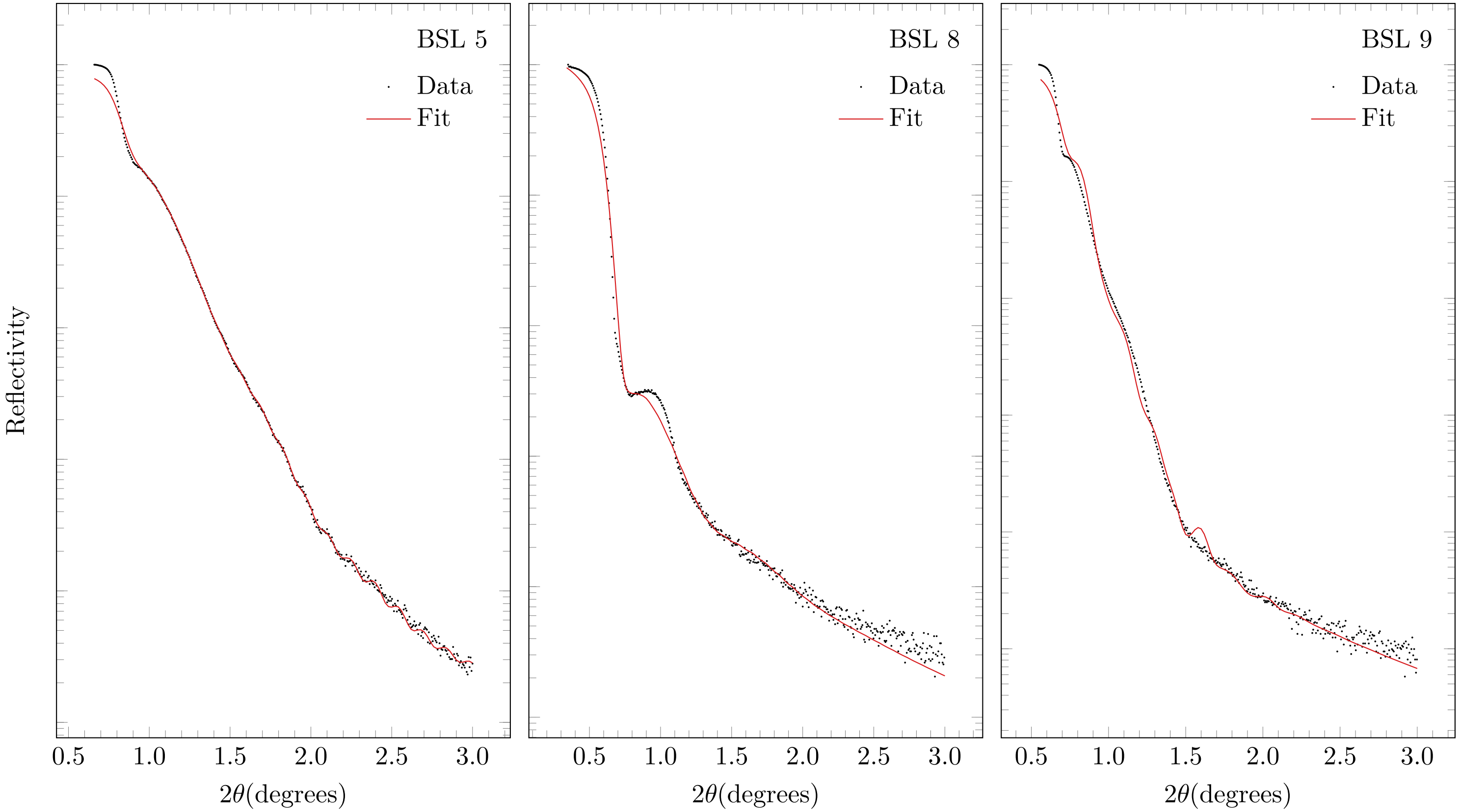
BSL 5
Data
Fit
BSL 8
Data
Fit
BSL 9
Data
Fit
Reflectivity
0.5
1.0
1.5
2.0
2.5
3.0
2θ(degrees)

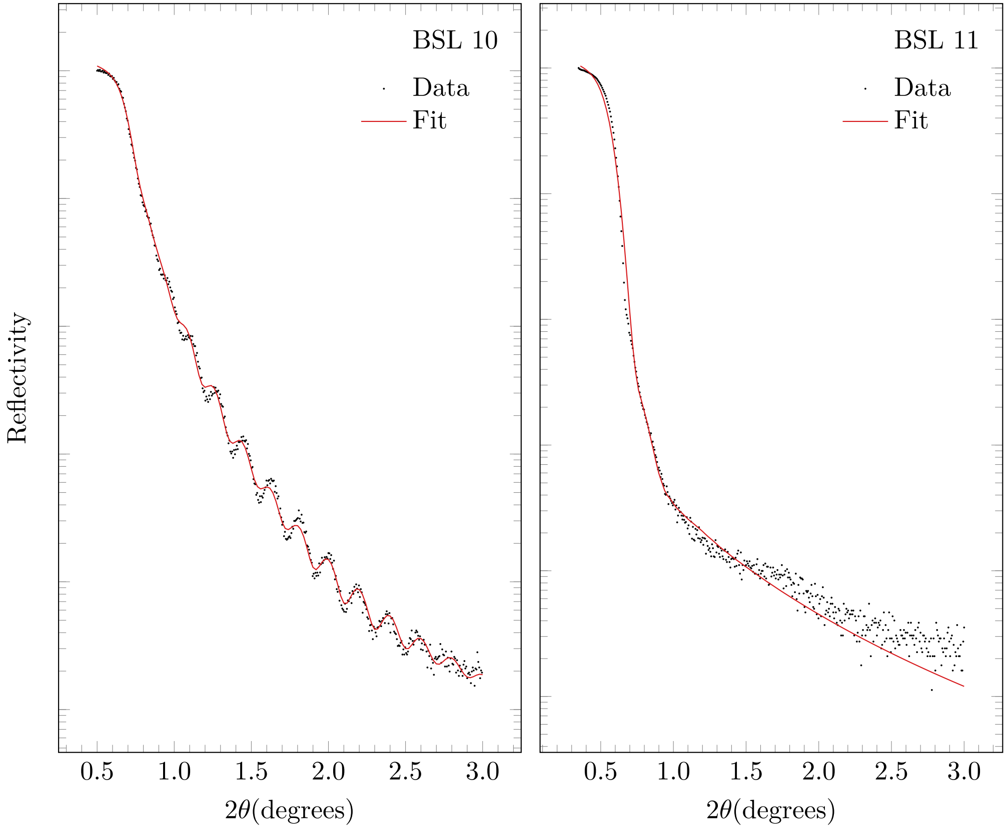

Figure 19: Fitted small-angle X-ray scattering spectra of the BSL samples.

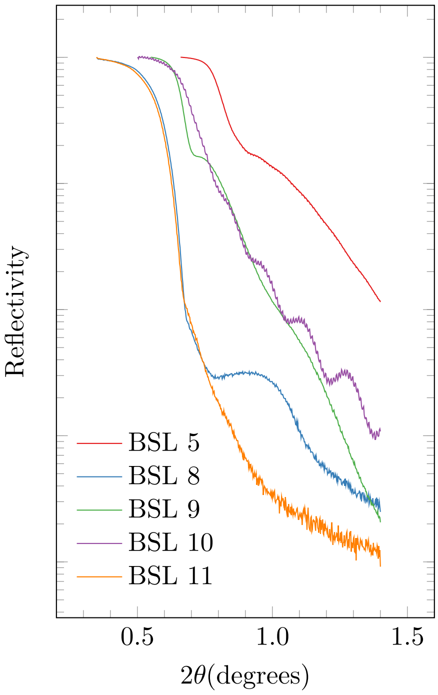

Figure 20: Comparison of the critical angle between the samples.

referred previously, the critical angle only depends on the density for these XRD measurements with fixed monochromatic radiation. Thus, we adjusted the densities of the thin film layers as necessary to have the corresponding critical angles on the computed reflectivity curve.

The minimisation algorithm needs a χ^2 for the calculations. If we simply use the square differences for the residues, the points at smaller angles with higher intensity will be over weighted. These points are less important to obtain information than the points at higher angles, where the fringes are more discernible. So, to compensate this, we calculate the residues as a difference of logarithms for N data points,

$$residue = \sum_{j=1}^{N} \left[\log_{10}\left(R_{exp,j}\right) - \log_{10}\left(R_{teo,j}\right)\right]^2 \tag{37}$$

, where $R_{exp,i}$ and $R_{teo,i}$ are, respectively, the experimental and theoretical reflectivities. This way, the solver can more easily obtain an accurate fit, especially of the Kiessig fringes, that have small amplitudes.

To perform the fits, we let the solver vary only three parameters: thickness, density and the interface roughness, for the different layers of the thin film. The resulting graphics of the minimizations are displayed in section 3.5 (on pages 34 and 35) and the obtained values are in table 6 (on page 37).

We expect that the fits for the samples 5, 8 and 10 are more reliable thanks to the presence of more clearly visible features (fringes, “bumps” in the spectra) that are due to less roughness. Consequently, the observed roughnesses in these samples are around 1 to 2 nm, see table 6.

Table 6: Summary of the obtained fit results for SAXS of the BSL samples.

Sample	Layer	f_r	f_i	t(nm)	σ(nm)	ρ(nm^{-3})
BSL 5	LSMO	98.3376	10.1012	45.16	1.32	23.5
	STO	84.0418	3.8204	7.38	1.78	24.0
	BLFO	125.9580	12.6733	4.36	1.14	24.6
BSL8	LSMO	98.3376	10.1012	86.80	1.26	7.6
	STO	84.0418	3.8204	9.97	1.18	13.6
	BLFO	125.9580	12.6733	20.72	6.45	10.3
BSL9	LSMO	98.3376	10.1012	38.60	2.15	10.1
	STO	84.0418	3.8204	16.25	2.15	28.9
	BLFO	125.9580	12.6733	22.78	2.20	12.7
BSL10	LSMO	98.3376	10.1012	43.25	1.17	8.5
	STO	84.0418	3.8204	17.21	7.71	26.0
	BLFO	125.9580	12.6733	20.56	1.96	12.1
BSL11	LSMO	98.3376	10.1012	120.13	3.32	7.3
	STO	84.0418	3.8204	17.67	2.82	3.4
	BLFO	125.9580	12.6733	46.57	5.15	9.3

WIDE-ANGLE X-RAY MODEL

Dynamic diffraction theory allows an accurate description of the interaction between radiation and periodic multilayer thin films. However, thin films without imperfections that destroy the periodicity are rare. In those cases, a kinematic approximation provides a simpler and better-suited interpretation of the diffraction patterns used for the structural determination. Knowing this, Fullerton et al. [1] and Meng et al. [2] followed a kinematic approach to describe the WAXS spectra of disordered multilayer thin films, for wide scattering angles, typically $2\theta > 10°$. Their formulation is for multilayer systems that are composed of repeating bilayers, whereas we want to analyse trilayer samples. As such, we followed a similar approach to theirs, but for an arbitrary number of different layers. See fig. 21 for a comparison of the type of multilayer each kinematic model deals with. We assumed the multilayer structure has continuous cumulative disorders both intralayer and interlayer, namely in the number of atomic planes, the spacing between them and the interfacial spacing.

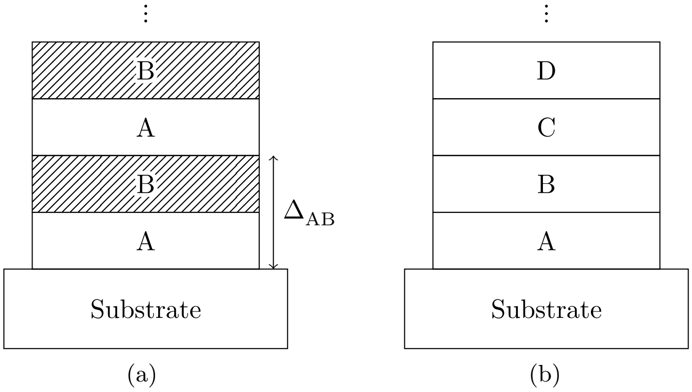

(a) (b)

Figure 21: Types of multilayer structures the kinematic models tries to model. (a) Repeated bilayer structure with period Δ_{AB} described by Fullerton and Meng's model. (b) Generic multilayer described by our model.

We will develop the model to describe the SAXS of a multilayer system that consists of a stack of N monolayers, labelled by an index j, on top of a semi-infinite substrate. Each layer consists of a stack of N_j atomic planes that share the same characteristic atomic scattering factor f_j, that describes how a material scatters incident radiation. These planes, labelled by an index k, are spaced from each other by d_{jk}. Between adjacent layers exists an interface, with an atomic spacing ξ_j that is distinct from the spacings inside each of those layers.

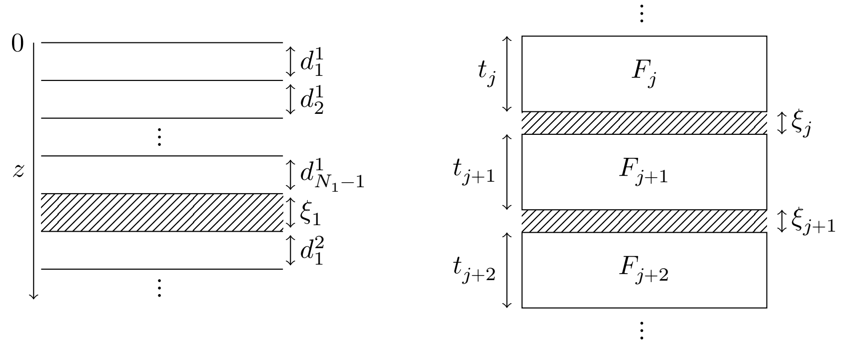

(a) (b)

Figure 22: Representation of a multilayer structure system. (a) A depiction of the multilayer structure at the atomic planes level. The structure is made of N_j atomic planes separated by d_{jk}. (b) A depiction of the multilayer structure at the layers level. The structure is composed by a stack of N layers of materials with structure factors F_j and thicknesses t_j, separated by interface atomic spacing ξ_j.

Each layer has a thickness t_j that is the summation of the all spacings between the atomic planes that compose the stack,

$$t_j = \sum_{k=1}^{N_j-1} d_{jk} \tag{38}$$

We can rewrite it if we use the average atomic spacing $\bar{d}_j$ in the layer,

$$t_j = \bar{d}_j(N_j - 1) \tag{39}$$

This way, we don't need to know the value of each individual atomic spacing but only the average value in the layer.

In this chapter, we will develop and apply a model that permits the description of WAXS spectra of disordered multilayers. We will start by obtaining the formula for an ideal multilayer, without disorder, in section 4.1. In each of the three subsequent sections, we add a new disorder to the multilayer. We begin with the disorder in the spacing between atomic planes in the layers, in section 4.2. After that, we add disorder to the interface's atomic spacing, in section 4.3. Lastly, we add disorder to the number of atomic planes, in section 4.4. The deduction is extensive, hence we have a summary with the necessary formulae for the determination of the WAXS intensity spectrum, in section 4.5. Finally, we fit the diffractograms of our five BSL multilayer samples with the obtained model, in section 4.6.

4.1 IDEAL MODEL

The basic model to describe WAXS for a one-dimensional multilayer is the "step" model[106]. The model assumes the samples are structures with abrupt composition changes across the interfaces, as seen in fig. 22.

The structure factor F describes how a material scatters the incident radiation[5], namely the amplitude and phase of the scattered wave. Although the multilayer crystal has a single structure factor, each layer j has its own characteristic structure factor F_j. The total scattered intensity by the crystal $I(q)$, both diffuse and specular, is determined by the square of the structure factor[1, 107],

$$I(q) = \langle F^*(q)F(q)\rangle \tag{40}$$

The average intensity requires the calculation of $\langle F^*(q)F(q)\rangle$, not $\langle F^*(q)\rangle\langle F(q)\rangle$[1]. The brackets represent an ensemble average over all possible variables, namely f_j, d_{jk}, N_j and ξ_j.

The structure factor for the whole superlattice is given by the function,

$$F(q) = F_1 + \sum_{j=2}^{N} F_j e^{-iq\sum\limits_{k=1}^{j-1}(t_k+\xi_k)} \tag{41}$$

For an ideal crystal, that does not take into account fluctuations from the average lattice, we do not need to average the intensity,

$$I(q) = \langle F^*(q)F(q)\rangle = F^*(q)F(q) \tag{42}$$

We just need to square the structure factor of the multilayers defined in eq. (41),

$$\begin{align} I(q) &= |F_1|^2 + \sum_{j'=2}^{N} A_{1j'} + \sum_{j'=2}^{N} A^*_{1j'} + \sum_{j=2}^{N}\sum_{j'=2}^{N} B_{jj'} \tag{43} \\ &= |F_1|^2 + 2\sum_{j'=2}^{N} \Re[A_{1j'}] + \sum_{j=2}^{N}\sum_{j'=2}^{N} B_{jj'} \tag{44} \end{align}$$

, with

$$\begin{align} A_{jj'} &\equiv F^*_j F_{j'} e^{-iq\sum\limits_{k=j}^{j'-1} t_k+\xi_k} \tag{45} \\ B_{jj'} &\equiv F^*_j F_{j'} e^{+iq\left[\sum\limits_{k=1}^{j-1} t_k+\xi_k - \sum\limits_{k=1}^{j'-1} t_k+\xi_k\right]} \tag{46} \end{align}$$

We will separate the double summation of $B_{jj'}$ in three regions: $j = j'$, $j > j'$ and $j < j'$,

$$\sum_{j=2}^{N}\sum_{j'=2}^{N} B_{jj'} = \sum_{j=2}^{N} B_{jj} + \sum_{j>j'}^{N}\sum_{j'=2}^{N-1} B_{jj'} + \sum_{j=2}^{N-1}\sum_{j'>j}^{N} B_{jj'} \tag{47}$$

The complex conjugate of the second term is:

$$\sum_{j>j'}^{N}\sum_{j'=2}^{N-1} B^*_{jj'} = \sum_{j>j'}^{N}\sum_{j'=2}^{N-1} F_j F^*_{j'} e^{-iq\left[\sum_{k=1}^{j-1} t_k+\xi_k-\sum_{k=1}^{j'-1} t_k+\xi_k\right]} \tag{48}$$

$$= \sum_{j>j'}^{N}\sum_{j'=2}^{N-1} F^*_{j'} F_j e^{+iq\left[\sum_{k=1}^{j'-1} t_k+\xi_k-\sum_{k=1}^{j-1} t_k+\xi_k\right]} \tag{49}$$

$$= \sum_{j>j'}^{N}\sum_{j'=2}^{N-1} B_{j'j} \tag{50}$$

We can swap j and j' because they are interchangeable indices,

$$\sum_{j>j'}^{N}\sum_{j'=2}^{N-1} B_{j'j} = \sum_{j=2}^{N-1}\sum_{j'>j}^{N} B_{jj'} = \sum_{j>j'}^{N}\sum_{j'=2}^{N-1} B^*_{jj'} \tag{51}$$

Now, the last two terms share the same summation indices and the terms are the complex conjugate of each other,

$$\sum_{j=2}^{N}\sum_{j'=2}^{N} B_{jj'} = \sum_{j=2}^{N} B_{jj} + \sum_{j=2}^{N-1}\sum_{j'>j}^{N} B_{jj'} + \sum_{j=2}^{N-1}\sum_{j'>j}^{N} B^*_{jj'} \tag{52}$$

$$= \sum_{j=2}^{N} B_{jj} + \sum_{j=2}^{N-1}\sum_{j'>j}^{N} \left[B_{jj'} + B^*_{jj'}\right] \tag{53}$$

$$= \sum_{j=2}^{N} B_{jj} + 2\sum_{j=2}^{N-1}\sum_{j'>j}^{N} \Re\left[B_{jj'}\right] \tag{54}$$

In the case of $j = j'$, as in the first term of eq. (54), the exponent in $B_{jj'}$ is zero, thus,

$$\sum_{j=2}^{N} B_{jj} = \sum_{j=2}^{N} F^*_j F_j = \sum_{j=2}^{N} \left|F_j\right|^2 \tag{55}$$

Now we will deal with the second term with the summation region, $j' > j$,

$$\sum_{j=2}^{N-1}\sum_{j'>j}^{N} \Re\left[B_{jj'}\right] = \sum_{j=2}^{N-1}\sum_{j'>j}^{N} \Re\left[F^*_j F_{j'} e^{iq\left[\sum_{k=1}^{j-1} t_k+\xi_k-\sum_{k=1}^{j'-1} t_k+\xi_k\right]}\right] \tag{56}$$

The exponent summations share the same terms, they just have different limits. However, the summation forces $j' > j$, so, we can unite the exponent summations into a single summation,

$$\sum_{j=2}^{N-1}\sum_{j'>j}^{N} \Re\left[B_{jj'}\right] = \sum_{j=2}^{N-1}\sum_{j'>j}^{N} \Re\left[F^*_j F_{j'} e^{-iq\sum_{k=j}^{j'-1} t_k+\xi_k}\right] \tag{57}$$

$$= \sum_{j=2}^{N-1}\sum_{j'>j}^{N} \Re\left[A_{jj'}\right] \tag{58}$$

We obtain an $A_{jj'}$ term that we can combine with the $A_{1j'}$ already presented in eq. (44). Putting them together, we get the scattering intensity for a perfect crystal,

$$I(q) = \sum_{j=1}^{N} |F_j|^2 + 2\sum_{j=1}^{N-1}\sum_{j'>j}^{N} \Re[A_{jj'}] \tag{59}$$

$$= \sum_{j=1}^{N} |F_j|^2 + 2\sum_{j=1}^{N-1}\sum_{j'>j}^{N} \Re\left[F_j^* F_{j'} e^{-iq\sum_{k=j}^{j'-1} t_k + \xi_k}\right] \tag{60}$$

As we can see from eq. (60), the scattered intensity for a multilayer crystal without defects is the summation of the scattered intensities of the individual layers plus interference terms if the crystal has more than one layer. All the information necessary about the materials and lattice is contained in the layer's structure factor F_j.

The layer's structure factor depends on the materials, type of lattice and crystallinity. Each layer is composed of an integer number N_j of atomic planes separated by a constant lattice spacing d_{jk}. The structure factor of such layers can be written, for a direction perpendicular to the surface, as:[2, 5, 17, 108]

$$F_j(q) = \sum_{k=0}^{N_j-1} f_{jk} e^{-iqkd_{jk}} \tag{61}$$

, where q is the modulus of the scattering vector,

$$q = 4\pi \sin\theta/\lambda \tag{62}$$

, for a scattering angle θ and an incident radiation wavelength λ. We are dealing with the reflection for one dimension, because of that, we can use the modulus of the scattering vector.

In eq. (61), each atom has its atomic scattering factor f_{jk}. This scattering factor only depends on the internal structure of the ion. Identical ions have identical form factors, regardless of their position[5].

Although the layers are polyatomic, we will consider that each layer is described by a single average scattering factor f_j. Defined as the average scattering factor in a unit cell of the material that composes the layer. We can follow the same logic for the crystal atomic spacing d_{jk} and assume it is constant in the layer, described by the layer's mean value $\bar{d}_j$. In that case, eq. (61) can be simplified,

$$F_j(q) = f_j \sum_{k=0}^{N_j-1} e^{-iqk\bar{d}_j} \tag{63}$$

Now that the atomic spacing is constant in the summation, the summation becomes a geometric series. The sum of the first n terms of a geometric series is:

$$\sum_{i=p}^{q} a^i = \frac{a^p - a^{q+1}}{1-a} \qquad \text{, for } a \neq 1 \text{ and } p, q \in \mathbb{N} \tag{64}$$

Thus, we can rewrite the layer's structure factor as:

$$F_j(q) = f_j \frac{1 - e^{-iqN_j\bar{d}_j}}{1 - e^{-iq\bar{d}_j}} \tag{65}$$

With eqs. (60) and (65) we can fully compute the WAXS intensity for an ideal multilayer.

Now we will use the intensity for a perfect crystalline multilayer and add the fluctuations we desire, namely, in the interplanar atomic distances, the thickness of the interfaces and the number of atomic planes. We will consider these three variables as physically independent and random. Gaussian distributions will describe the randomness of these variables. Because the variables are independent, we can compute the averages over each parameter separately.

4.2 ATOMIC SPACING FLUCTUATION

In an ideal crystal, the layers' atomic spacing are well defined and thanks to that the radiation is scattered at specific angles related with those spacings. However, a real crystal has defects that can change the spacing between atomic planes. This causes a broadening and reduction of intensity of the scattered peaks. To take that into account, we will not deal with the absolute atomic spacings but their deviation from the mean value. So, we will consider that each atomic spacing d_{jk} with index k inside a layer j is shifted from the mean value $\bar{d}_j$ by a random amount Δ_{jk}, as seen in fig. 23.

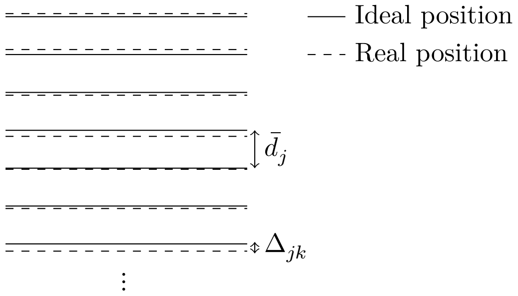

Figure 23: The atomic planes are shifted by Δ_{jk} from their ideal positions, due to disorder.

The shift is related with the mean and real spacing,

$$\Delta_{jk} \equiv d_{jk} - \bar{d}_j \tag{66}$$

Now we need rewrite the structure factor from the ideal crystal, eq. (41), to take into account the fluctuations in the atomic spacing by adding all the fluctuations to the travelled distance,

$$F(q) = F_1 + \sum_{j=2}^{N} F_j e^{-iq\sum_{k=1}^{j-1}\left[t_k + \xi_k + \sum_{r=1}^{N_k-1}\Delta_{kr}\right]} \tag{67}$$

Once again, the intensity is determined by the square of the structure factor,

$$I(q) = \sum_{j=1}^{N} |F_j|^2 + 2\sum_{j=1}^{N-1}\sum_{j'>j}^{N} \Re\left[A'_{jj'}\right] \tag{68}$$

, with

$$A'_{jj'} \equiv F_j^* F_{j'} e^{-iq\sum_{k=j}^{j'-1}\left[t_k + \xi_k + \sum_{r=1}^{N_k-1}\Delta_{kr}\right]} \tag{69}$$

$$= F_j^* F_{j'} e^{-iq\sum_{k=j}^{j'-1}\left[t_k + \sum_{r=1}^{N_k-1}\Delta_{kr}\right]} e^{-iq\sum_{k=j}^{j'-1}\xi_k} \tag{70}$$

We can separate $A'_{jj'}$ in two terms, one that depends on Δ_{jk} and other that depends on ξ_j,

$$A'_{jj'} \equiv A^{\Delta}_{jj'} A^{\xi}_{jj'} \tag{71}$$

, with

$$A^{\Delta}_{jj'} \equiv F_j^* F_{j'} e^{-iq\sum_{k=j}^{j'-1}\left[t_k + \sum_{r=1}^{N_k-1}\Delta_{kr}\right]} \tag{72}$$

$$A^{\xi}_{jj'} \equiv e^{-iq\sum_{k=j}^{j'-1}\xi_k} \tag{73}$$

This separation will allow us to average the terms individually. We will not need to average $A^{\Delta}_{jj'}$ in order to ξ_j and we also will not need to average $A^{\xi}_{jj'}$ in order to Δ_{jk}.

The intensity depends on two terms. The first is the non-crossed intensity I_{nc} that is the summation of the intensities from each layer. The second term is the crossed intensities I_c that gives the interference that occurs between interfaces. Therefore the intensity can be rewritten as,

$$I(q) = \sum_{j=1}^{N} |F_j|^2 + 2\sum_{j=1}^{N-1}\sum_{j'>j}^{N} \Re\left[A^{\xi}_{jj'} A^{\Delta}_{jj'}\right] \tag{74}$$

$$= I_{nc} + I_c \tag{75}$$

, with

$$I_{nc}(q) \equiv \sum_{j=1}^{N} |F_j|^2 \tag{76}$$

$$I_c(q) \equiv 2\sum_{j=1}^{N-1}\sum_{j'>j}^{N} \Re\left[A^{\xi}_{jj'} A^{\Delta}_{jj'}\right] \tag{77}$$

As should be expected, only the crossed terms depend on the interface thickness ξ_j, that is present in $A^{\xi}_{jj'}$.

Now that we know the intensity, we will integrate it in order of the the atomic spacing fluctuations Δ_{jk} to obtain the average intensity,

$$
\begin{aligned}
I(q) = \langle I(q) \rangle &= \left\langle F_j^* F_j \right\rangle_{\Delta} &(78)\\
&= \sum_{j=1}^{N} \left\langle |F_j|^2 \right\rangle_{\Delta} + 2 \sum_{j=1}^{N-1} \sum_{j'>j}^{N} \Re\left[\left\langle A'_{jj'} \right\rangle_{\Delta} \right] &(79)\\
&= \sum_{j=1}^{N} \left\langle |F_j|^2 \right\rangle_{\Delta} + 2 \sum_{j=1}^{N-1} \sum_{j'>j}^{N} \Re\left[\left\langle A^{\xi}_{jj'} A^{\Delta}_{jj'} \right\rangle_{\Delta} \right] &(80)
\end{aligned}
$$

As referred previously, $A^{\xi}_{jj'}$ doesn't depend on Δ_{jk}, as such, it is constant on the ensemble average over Δ_{jk},

$$
I(q) = \sum_{j=1}^{N} \left\langle |F_j|^2 \right\rangle_{\Delta} + 2 \sum_{j=1}^{N-1} \sum_{j'>j}^{N} \Re\left[A^{\xi}_{jj'} \left\langle A^{\Delta}_{jj'} \right\rangle_{\Delta} \right] \tag{81}
$$

The layers' structure factor F_j depends on the atomic spacing. Therefore, we also need to change it to take into account the fluctuations in the atomic spacing. We will denominate these new structure factors as F'_j to differentiate from the structure factors from the perfect crystal. The new structure factors are:

$$
F'_j(q) = f_j \sum_{k=0}^{N_j-1} e^{-iq(\bar{d}_j k + \sum_{r=1}^{k} \Delta_{kr})} \tag{82}
$$

Now that we know the structure factors, we can determine $|F'_j|^2$ from the non-crossed intensity,

$$
\begin{aligned}
|F'_j|^2 &= F'^{*}_j F'_{j'} &(83)\\
&= \left| f_j \right|^2 \sum_{k=0}^{N_j-1} \sum_{k'=0}^{N_j-1} e^{-iq\left[\bar{d}_j (k'-k) + \sum_{r=1}^{k'} \Delta_{k'r} - \sum_{r=1}^{k} \Delta_{kr} \right]} &(84)
\end{aligned}
$$

For simplicity we will define the function

$$
C_{kk'} \equiv e^{-iq\left[\bar{d}_j (k'-k) + \sum_{r=1}^{k'} \Delta_{k'r} - \sum_{r=1}^{k} \Delta_{kr} \right]} \tag{85}
$$

We separate the summations from eq. (84) into three different limits: $k = k'$, $k > k'$ and $k < k'$,

$$
|F'_j|^2 = \left| f_j \right|^2 \left[\sum_{k=0}^{N_j-1} C_{kk} + \sum_{k=0}^{N_j-2} \sum_{k'>k}^{N_j-1} C_{kk'} + \sum_{k>k'}^{N_j-1} \sum_{k'=0}^{N_j-2} C_{kk'} \right] \tag{86}
$$

For $k = k'$, the exponent of C_{kk}, defined in eq. (85), is zero, thus,

$$
\sum_{k=0}^{N_j-1} C_{kk} = N_j \tag{87}
$$

For $k > k'$, we can transform the the term in a similar fashion to eq. (50),

$$\sum_{k>k'}^{N_j-1}\sum_{k'=0}^{N_j-2} C^*_{kk'} = \sum_{k>k'}^{N_j-1}\sum_{k'=0}^{N_j-2} e^{+iq\left[\bar{d}_j(k'-k)+\sum_{r=1}^{k'}\Delta_{k'r}-\sum_{r=1}^{k}\Delta_{kr}\right]} \tag{88}$$

$$= \sum_{k>k'}^{N_j-1}\sum_{k'=0}^{N_j-2} e^{-iq\left[\bar{d}_j(k-k')+\sum_{r=1}^{k}\Delta_{kr}-\sum_{r=1}^{k'}\Delta_{k'r}\right]} \tag{89}$$

$$= \sum_{k>k'}^{N_j-1}\sum_{k'=0}^{N_j-2} C_{k'k} \tag{90}$$

The k and k' indices are interchangeable, so,

$$\sum_{k=0}^{N_j-2}\sum_{k'>k}^{N_j-1} C_{kk'} = \sum_{k>k'}^{N_j-1}\sum_{k'=0}^{N_j-2} C_{k'k} = \sum_{k>k'}^{N_j-1}\sum_{k'=0}^{N_j-2} C^*_{kk'} \tag{91}$$

Replacing eqs. (87) and (91) into eq. (86),

$$|F'_j|^2 = \left|f_j\right|^2 \left[N_j + \sum_{k=0}^{N_j-2}\sum_{k'>k}^{N_j-1} C_{kk'} + \sum_{k=0}^{N_j-2}\sum_{k'>k}^{N_j-1} C^*_{kk'}\right] \tag{92}$$

$$= \left|f_j\right|^2 \left[N_j + 2\Re\left[\sum_{k=0}^{N_j-2}\sum_{k'>k}^{N_j-1} C_{kk'}\right]\right] \tag{93}$$

The summations of $C_{kk'}$ have the condition that $k > k'$, because of that, we can simplify the exponent in $C_{kk'}$, defined in eq. (85), if we combine the Δ_{jk} summations,

$$C_{kk'} = e^{-iq\left[\bar{d}_j(k'-k)+\sum_{r=k+1}^{k'}\Delta_{k'r}\right]} \tag{94}$$

Averaging eq. (86) over Δ_{jk} we get

$$\left\langle |F'_j|^2 \right\rangle_{\Delta} = \left|f_j\right|^2 \left[N_j + 2\Re\left[\sum_{k=0}^{N_j-2}\sum_{k'>k}^{N_j-1} \langle C_{kk'}\rangle_{\Delta}\right]\right] \tag{95}$$

, where $\langle C_{kk'}\rangle$ is defined as:

$$\sum_{k=0}^{N_j-2}\sum_{k'>k}^{N_j-1} \langle C_{kk'}\rangle_{\Delta} = \sum_{k=0}^{N_j-2}\sum_{k'>k}^{N_j-1} e^{-iqd_j(k'-k)} \left\langle e^{-iq\sum_{r=k+1}^{k'}\Delta_{k'r}} \right\rangle_{\Delta} \tag{96}$$

We can transform the exponential of a summation in a product of exponentials,

$$e^{\sum_{i=p}^{q} a_i} = \prod_{i=p}^{q} e^{a_i} \tag{97}$$

We will consider the atomic spacing fluctuations as physically independent, therefore, we can calculate the mean of each term of the product separately,

$$\left\langle \prod_{r=k+1}^{k'} e^{-iq\Delta_{k'r}} \right\rangle_{\Delta} = \left\langle e^{-iq\Delta_{k',k+1}} \right\rangle_{\Delta} \times \left\langle e^{-iq\Delta_{k',k+2}} \right\rangle_{\Delta} \times \cdots \tag{98}$$

Random variables are described by their probability distribution, which specifies the probability that its value falls in any given interval. Real-valued independent random variables are described by normalised Gaussian (normal) distributions. The probability density of a Gaussian distribution is:

$$P(x) = Ae^{-(x-\bar{x})/2\sigma_x^2} \qquad , \text{ for } \sigma > 0 \tag{99}$$

, where x is the random variable, $\bar{x}$ and σ_x are, respectively, its mean and standard deviation and A it is a normalization constant. The normalisation constant depends on the random variable bound. To obtain the constant we normalise the distribution in the bound limit $[p, q]$[109],

$$A \int_p^q e^{-(x-\bar{x})/2\sigma_x^2} \, \mathrm{d}x = 1 \tag{100}$$

Every Gaussian distribution is an exponential with a quadratic exponent. The primitive of this type of functions is given by Gradshteyn's [110],

$$\int e^{-(ax^2+2bx+c)} \, \mathrm{d}x = \frac{1}{2}\sqrt{\frac{\pi}{a}} e^{(b^2-ac)/a} \operatorname{erf}\left(\frac{xa+b}{\sqrt{a}} \right) + \text{const.} \tag{101}$$

, for $a \neq 0$. Thus, the primitive of the Gaussian distribution's exponential defined in eq. (99) is:

$$\int e^{-(x-\bar{x})^2/2\sigma^2} \, \mathrm{d}x = \frac{1}{2}\sqrt{2\pi\sigma^2} \operatorname{erf}\left(\frac{x-\bar{x}}{\sqrt{2\sigma^2}} \right) + const. \tag{102}$$

, with an integral in the interval $[p, q]$:

$$\int_p^q e^{-(x-\bar{x})^2/2\sigma^2} \, \mathrm{d}x = \frac{1}{2}\sqrt{2\pi\sigma^2} \left[\operatorname{erf}\left(\frac{q-\bar{x}}{\sqrt{2\sigma^2}} \right) - \operatorname{erf}\left(\frac{p-\bar{x}}{\sqrt{2\sigma^2}} \right) \right] \tag{103}$$

These integrals depend on the error function erf(x), that is defined as[110]:

$$\operatorname{erf}(x) \equiv \frac{2}{\sqrt{\pi}} \int_0^x e^{-y^2} \, \mathrm{d}y \tag{104}$$

The error function exhibits an asymptotic behaviour, with two horizontal asymptotes,

$$\lim_{x\to-\infty} \operatorname{erf}(x) = -1$$
$$\lim_{x\to+\infty} \operatorname{erf}(x) = +1$$

The asymptotic behaviour is visible in the error function plot in fig. 24

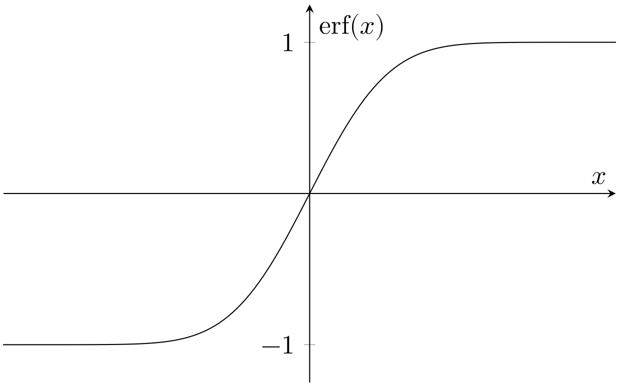

Figure 24: Error function erf(x).

The error function also exhibits an odd parity, that is $-\operatorname{erf}(x) = \operatorname{erf}(-x)$, which we can exploit to rewrite the primitive's result,

$$\int_p^q e^{-(x-\bar{x})^2/2\sigma^2}\,\mathrm{d}x = \frac{\sqrt{2\pi\sigma^2}}{2}\left[\operatorname{erf}\left(\frac{q-\bar{x}}{\sqrt{2\sigma^2}}\right) + \operatorname{erf}\left(-\frac{p-\bar{x}}{\sqrt{2\sigma^2}}\right)\right] \tag{105}$$

Knowing the asymptotic behaviour of the error function, we can normalise the Gaussian distribution for a random variable that can take any real-value,

$$A\int_{-\infty}^{+\infty} e^{-(x-\bar{x})^2/2\sigma^2}\,\mathrm{d}x = 1 \tag{106}$$

$$A = \frac{1}{\sqrt{2\pi\sigma^2}} \tag{107}$$

So, the normalised Gaussian distribution in the $(-\infty, +\infty)$ region is:

$$P(x) = \frac{e^{-(x-\bar{x})/2\sigma_x^2}}{\sqrt{2\pi\sigma^2}} \tag{108}$$

As we are dealing with deviations from the average interatomic distances, the distribution is centred around 0. The deviation should also have a lower limit like the atomic spacing. However, the deviation should be well below the atomic spacing. So, it should not affect much the result. This means that the distribution is not truncated, which simplifies the integration result. With this specifications, the deviation from the atomic spacing average is defined by the following probability distribution:

$$P(\Delta_{jk}) = \frac{e^{-(\Delta_{jk}-\bar{d}_j)/2\sigma^2_{\Delta j}}}{\sqrt{2\pi\sigma^2_{\Delta j}}} \tag{109}$$

Now that we know the atomic spacing fluctuations probability distribution we can determine the terms of the product from eq. (98). In these terms, the only variable is the atomic spacing fluctuation Δ_{jk}. For an arbitrary layer j and spacing k, the term is

$$\left\langle e^{-iq\Delta_{jk}} \right\rangle_{\Delta} = \int\limits_{-\infty}^{\infty} P(\Delta_{jk}) e^{-iq\Delta_{jk}}\, \mathrm{d}\Delta_{jk} \tag{110}$$

The result of this integral for a Gaussian distribution is given by eq. (105),

$$\left\langle e^{-iqx} \right\rangle_{x} = \int\limits_{-\infty}^{\infty} e^{-a^2(x-\bar{x})^2} e^{-iqx}\, \mathrm{d}x \tag{111}$$

$$= \sqrt{\frac{\pi}{a}} e^{-q^2/4a^2} e^{-iq\bar{x}} \tag{112}$$

, this result is important, since it will appear again when we average in relation to the remaining variables. For now, let's solve eq. (110),

$$\left\langle e^{-iq\Delta_{jk}} \right\rangle_{\Delta} = e^{-q^2\sigma^2_{\Delta j}/2} \tag{113}$$

As we can see it no longer depends on the atomic spacing fluctuation Δ_{jk}. It depends only on its variance $\sigma^2_{\Delta j}$, that is the same in each layer. Therefore, all terms from eq. (98) are the same in a layer j. As such, the product from eq. (98) for spacing with index k' is:

$$\left\langle \prod_{r=k+1}^{k'} e^{-iq\Delta_{k'r}} \right\rangle_{\Delta} = \prod_{r=k+1}^{k'} \left\langle e^{-iq\Delta_{jk}} \right\rangle_{\Delta} \tag{114}$$

$$= \prod_{r=k+1}^{k'} e^{-q^2\sigma^2_{\Delta j}/2} \tag{115}$$

$$= e^{-q^2\sigma^2_{\Delta j}(k'-k)/2} \tag{116}$$

Knowing the result from eq. (116), we can determine the average non-crossed intensity with atomic spacing fluctuations. The average intensity from eq. (95) becomes:

$$\left\langle |F'_j|^2 \right\rangle_{\Delta} = |f_j|^2 \left[N_j + 2\Re\left[\sum_{k=0}^{N_j-2} \sum_{k'>k}^{N_j-1} e^{-(k'-k)\beta^{\Delta}_j} \right] \right] \tag{117}$$

, where

$$\beta_j^\Delta \equiv \beta_{jr}^\Delta + i\beta_{ji}^\Delta \qquad \beta_{jr}^\Delta \equiv q^2\sigma_{\Delta j}^2/2 \qquad \beta_{ji}^\Delta \equiv q\bar{d}_j \tag{118}$$

As we can see from eq. (117), the average non-crossed intensity no longer depends on individual atomic spacing fluctuations Δ_{jk}, and we can fully describe those fluctuations by the mean $\bar{d}_j$ and variance $\sigma_{\Delta j}^2$ of each layer.

The double summation in eq. (117) is a geometric series. To resolve the geometric series we define the following variables,

$$K \equiv k' - k \tag{119}$$

Rewriting the exponential from eq. (117) with the eqs. (118) and (119), the geometric series becomes more clear,

$$\sum_{k=0}^{N_j-2}\sum_{K=1}^{N_j-1-k}\left[e^{-\beta_j^\Delta}\right]^K = \sum_{k=0}^{N_j-2}\frac{e^{-\beta_j^\Delta} - e^{-(N_j-k)\beta_j^\Delta}}{1-e^{-\beta_j^\Delta}} \tag{120}$$

$$= \frac{(N_j-1)e^{-\beta_j^\Delta} - \sum\limits_{k=0}^{N_j-2} e^{-(N_j-k)\beta_j^\Delta}}{1-e^{-\beta_j^\Delta}} \tag{121}$$

We will define another variable,

$$K' \equiv N_j - k \tag{122}$$

This variable transforms the remaining summation from eq. (121) in a geometric series,

$$\sum_{k=0}^{N_j-2}\left[e^{-\beta_j^\Delta}\right]^{N_j-k} = \sum_{K'=2}^{N_j}\left[e^{-\beta_j^\Delta}\right]^{K'} = \frac{e^{-2\beta_j^\Delta} - e^{-(N_j+1)\beta_j^\Delta}}{1-e^{-\beta_j^\Delta}} \tag{123}$$

Replacing the summation from eq. (121) with this geometric series, we get

$$\sum_{k=0}^{N_j-2}\sum_{K=1}^{N_j-1-k}\left[e^{-\beta_j^\Delta}\right]^K = \frac{(N_j-1)e^{-\beta_j^\Delta} - \dfrac{e^{-2\beta_j^\Delta} - e^{-(N_j+1)\beta_j^\Delta}}{1-e^{-\beta_j^\Delta}}}{1-e^{-\beta_j^\Delta}} \tag{124}$$

$$= \frac{N_j\left[e^{-\beta_j^\Delta} - e^{-2\beta_j^\Delta}\right] - e^{-\beta_j^\Delta} + e^{-(N_j+1)\beta_j^\Delta}}{\left[1-e^{-\beta_j^\Delta}\right]^2} \tag{125}$$

With the geometric series resolved we obtain the multilayer's average non-crossed intensity,

$$\langle I_{nc}\rangle_\Delta = \sum_{j=1}^{N}\left\langle |F_j'|^2\right\rangle_\Delta \tag{126}$$

$$= \sum_{j=1}^{N}\left|f_j\right|^2\left[N_j + 2\mathfrak{R}\left[\frac{N_j\left[e^{-\beta_j^\Delta} - e^{-2\beta_j^\Delta}\right] - e^{-\beta_j^\Delta} + e^{-(N_j+1)\beta_j^\Delta}}{\left[1-e^{-\beta_j^\Delta}\right]^2}\right]\right] \tag{127}$$

The non-crossed intensity no longer depends on individual atomic spacings k, and we lose all dependencies on individual atomic planes. The non-crossed intensity of a layer becomes fully described by only the layer parameters, namely, the total number of atomic planes N_j, the average atomic spacing $\bar{d}_j$ and variance $\sigma^2_{\Delta j}$ and the atomic scattering factor f_j.

We know the non-crossed intensity, but the crossed intensity still remains to be determined, which we will do in this subsection. The average crossed intensity with atomic spacing fluctuations is given by the second collection of terms in eq. (81). Only the averaging of $A^{\Delta}_{jj'}$ needs to be determined. $A^{\Delta}_{jj'}$ is given by eq. (72), averaging it we get

$$\left\langle A^{\Delta}_{jj'} \right\rangle_{\Delta} = \left\langle F'^{*}_{j} F'_{j'} e^{-iq \sum_{k=j}^{j'-1} \left[t_k + \sum_{r=1}^{N_k-1} \Delta_{kr} \right]} \right\rangle_{\Delta} \tag{128}$$

We can separate the summation in two, one with a single term $k = j$ and the other for the terms $k > j$,

$$\left\langle A^{\Delta}_{jj'} \right\rangle_{\Delta} = \left\langle F'^{*}_{j} e^{-iq \left[t_j + \sum_{r=1}^{N_j-1} \Delta_{jr} \right]} F'_{j'} e^{-iq \sum_{k>j}^{j'-1} \left[t_k + \sum_{r=1}^{N_k-1} \Delta_{kr} \right]} \right\rangle_{\Delta} \tag{129}$$

We can separate $A^{\Delta}_{jj'}$ into three terms, where each term only depends on one atomic plane index (j, j' or k). Each atomic plane scatters the radiation independently from the others. Therefore, we can average each of these terms separately,

$$\left\langle A^{\Delta}_{jj'} \right\rangle_{\Delta} = \left\langle F'_{j'} \right\rangle_{\Delta} \left\langle e^{-iq \sum_{k>j}^{j'-1} \left[t_k + \sum_{r=1}^{N_k-1} \Delta_{kr} \right]} \right\rangle_{\Delta} \left\langle F'^{*}_{j} e^{-iq \left[t_j + \sum_{r=1}^{N_j-1} \Delta_{jr} \right]} \right\rangle_{\Delta} \tag{130}$$

Now, we just need to determine each of these three averages. Starting by the average in the j' index. The structure factor of an individual layer is defined in eq. (82), averaging it in relation to the atomic spacings,

$$\left\langle F'_{j'} \right\rangle_{\Delta} = \left\langle f_{j'} \sum_{k'=0}^{N_{j'}-1} e^{-iq \left[k' \bar{d}_{j'} + \sum_{r=1}^{k'} \Delta_{j'r} \right]} \right\rangle_{\Delta} \tag{131}$$

$$= f_{j'} \sum_{k'=0}^{N_{j'}-1} e^{-ik' \beta^{\Delta}_{j'i}} \left\langle e^{-iq \sum_{r=1}^{k'} \Delta_{j'r}} \right\rangle_{\Delta} \tag{132}$$

The atomic spacing deviations are originated by intralayer disorder, that are assumed to be non-cumulative, the disorders in each plane is independent from the other planes. Assuming that all the $\Delta_{j'r}$ distributions have the same variance $\sigma^2_{\Delta j'}$ for a given layer,

$$\left\langle F'_{j'} \right\rangle_{\Delta} = f_{j'} \sum_{k'=0}^{N_{j'}-1} \left[e^{-ik'\beta^{\Delta}_{j'i}} \prod_{r=1}^{k'} \left\langle e^{-iq\Delta_{j'r}} \right\rangle \right] \tag{133}$$

$$= f_{j'} \sum_{k'=0}^{N_{j'}-1} \left[e^{-ik'\beta^{\Delta}_{j'i}} \prod_{r=1}^{k'} e^{-\beta^{\Delta}_{j'r}} \right] \tag{134}$$

$$= f_{j'} \sum_{k'=0}^{N_{j'}-1} \left[e^{-ik'\beta^{\Delta}_{j'i}} e^{-k'\beta^{\Delta}_{j'r}} \right] = f_{j'} \sum_{k'=0}^{N_{j'}-1} e^{-k'\beta^{\Delta}_{j'}} \tag{135}$$

Now $\langle F'_{j'} \rangle_{\Delta}$ is a geometric series, as such, we can rewrite it has

$$\left\langle F'_{j'} \right\rangle_{\Delta} = f_{j'} \frac{1 - e^{-N_{j'}\beta^{\Delta}_{j'}}}{1 - e^{-\beta^{\Delta}_{j'}}} \tag{136}$$

We will determine now the second mean term of the crossed terms. The layer thickness t_k, given by eq. (39), is independent from the intralayer fluctuations Δ_{jk} we can separate the summations

$$\left\langle e^{-iq\sum\limits_{k>j}^{j'-1}\left[t_k + \sum\limits_{r=1}^{N_k-1}\Delta_{kr}\right]} \right\rangle_{\Delta} = e^{-iq\sum\limits_{k>j}^{j'-1} t_k} \left\langle e^{-iq\sum\limits_{k>j}^{j'-1}\sum\limits_{r=1}^{N_k-1}\Delta_{kr}} \right\rangle_{\Delta} \tag{137}$$

All intralayer fluctuations are assumed to be independent, as such, we can do average each term individually.

$$\left\langle e^{-iq\sum\limits_{k>j}^{j'-1}\sum\limits_{r=1}^{N_k-1}\Delta_{kr}} \right\rangle_{\Delta} = \left\langle e^{-iq\Delta_{j+1,1}} \right\rangle_{\Delta} \times \left\langle e^{-iq\Delta_{j+1,2}} \right\rangle_{\Delta} \times \cdots \tag{138}$$

$$= e^{-\sum\limits_{k>j}^{j'-1}(N_k-1)\beta^{\Delta}_{kr}} \tag{139}$$

Replacing eq. (139) into eq. (137) and layer's thickness with the expression from eq. (39), we get

$$\left\langle e^{-iq\sum\limits_{k>j}^{j'-1}\left[t_k + \sum\limits_{r=1}^{N_k-1}\Delta_{kr}\right]} \right\rangle_{\Delta} = e^{-i\sum\limits_{k>j}^{j'-1}(N_k-1)\beta^{\Delta}_{ki}} e^{-\sum\limits_{k>j}^{j'-1}(N_k-1)\beta^{\Delta}_{kr}} \tag{140}$$

$$= e^{-\sum\limits_{k>j}^{j'-1}(N_k-1)\beta^{\Delta}_{k}} \tag{141}$$

Now we will calculate the last of the crossed average terms in relation to Δ_{jk}. First we will replace F'_j from eq. (82).

$$\left\langle F'^{*}_{j} e^{-iq\left[t_j + \sum\limits_{r=1}^{N_j-1}\Delta_{jr}\right]} \right\rangle_{\Delta} = \left\langle f^*_j \sum_{k=0}^{N_j-1} e^{+iq\left[k\bar{d}_j + \sum\limits_{r=1}^{k}\Delta_{jr}\right]} e^{-iq\left[t_j + \sum\limits_{r=1}^{N_j-1}\Delta_{jr}\right]} \right\rangle_{\Delta} \tag{142}$$

We take the terms that don't depend on Δ_{jk} out of the average. The exponential that are being average share the same terms and lower limit, so, we are calculating two times the summation with inferior upper limit,

$$\left\langle F_j'^{*} e^{-iq\left[t_j+\sum\limits_{r=1}^{N_j-1}\Delta_{jr}\right]}\right\rangle_{\Delta} = f_j^{*}\sum_{k=0}^{N_j-1} e^{-i(N_j-1-k)\beta_{ji}^{\Delta}} \times\left\langle e^{-iq\left[\sum\limits_{r=1}^{k}\Delta_{jr}-\sum\limits_{r=1}^{k}\Delta_{jr}+\sum\limits_{r=k+1}^{N_j-1}\Delta_{jr}\right]}\right\rangle_{\Delta} \tag{143}$$

We can resolve the average the same way we did in eq. (98) to 116, where we separate the exponential with summation exponent into a product of exponentials and average each term separately,

$$\left\langle e^{-iq\sum\limits_{r=k+1}^{N_j-1}\Delta_{jr}}\right\rangle_{\Delta} = e^{-(N_j-1-k)\beta_{jr}^{\Delta}} \tag{144}$$

Putting all together,

$$\left\langle F_j'^{*} e^{-iq\left[t_j+\sum\limits_{r=1}^{N_j-1}\Delta_{jr}\right]}\right\rangle_{\Delta} = f_j\sum_{k=0}^{N_j-1} e^{-i(N_j-1-k)\beta_{ji}^{\Delta}}e^{-(N_j-1-k)\beta_{jr}^{\Delta}} \tag{145}$$

$$= e^{-(N_j-1)\beta_j^{\Delta}} f_j^{*}\sum_{k=0}^{N_j-1} e^{+k\beta_j^{\Delta}} \tag{146}$$

We obtain a geometric series,

$$\left\langle F_j'^{*} e^{-iq\left[t_j+\sum\limits_{r=1}^{N_j-1}\Delta_{jr}\right]}\right\rangle_{\Delta} = f_j^{*}\frac{1-e^{+N_j\beta_j^{\Delta}}}{1-e^{+\beta_j^{\Delta}}}e^{-(N_j-1)\beta_j^{\Delta}} \tag{147}$$

$$= f_j^{*}\frac{e^{-(N_j-1)\beta_j^{\Delta}}-e^{+\beta_j^{\Delta}}}{1-e^{+\beta_j^{\Delta}}} \tag{148}$$

Putting together the crossed terms form eqs. (136), (141) and (148) we obtain the average crossed intensity in relation to Δ_{jk}.

$$\left\langle A_{jj'}^{\Delta}\right\rangle_{\Delta} = f_j^{*}f_{j'}\left[\frac{1-e^{+N_j\beta_j^{\Delta}}}{1-e^{+\beta_j^{\Delta}}}\right]\left[\frac{1-e^{-N_{j'}\beta_{j'}^{\Delta}}}{1-e^{-\beta_{j'}^{\Delta}}}\right]e^{-(N_j-1)\beta_j^{\Delta}-\sum\limits_{k>j}^{j'-1}(N_k-1)\beta_k^{\Delta}} \tag{149}$$

4.3 LATTICE-MISMATCHED INCOHERENT INTERFACE

If the lattice positions are not well defined, the atomic spacing in the interface will vary and create a lattice mismatch incoherent interface.

In an ideal crystal, the atomic spacing in the interface is the average between the atomic spacings of the adjacent layers. So, we will do a similar procedure as we did for the layers' atomic spacing, we will deal with the deviation ξ_k from the average $\bar{\xi}_j$ instead of the absolute value ξ_j. We will define the deviation as:

$$\xi_j = \xi_j - \bar{\xi}_j \tag{150}$$

The interface spacing is described by a Gaussian distribution with variance $\sigma^2_{\xi j}$,

$$P(\xi_k) = \frac{e^{-\xi_k^2/2\sigma^2_{\xi j}}}{\sqrt{2\pi\sigma^2_{\xi j}}} \tag{151}$$

All the random variables we will average are independent. Thus, we will average in order to ξ_k the previously obtained average intensity,

$$\langle I \rangle_{\Delta\xi} = \langle P(\xi_k) P(\Delta_{jk}) F^*(q) F(q) \rangle = \langle P(\xi_k) \langle I \rangle_{\Delta} \rangle \tag{152}$$

The non-crossed intensity is the summation of the scattered intensities, therefore, they don not depend on the interfaces. On the other hand, the crossed intensity depends on the interface spacing but the dependency is restricted to the term $A^{\xi}_{jj'}$, defined in eq. (73). Thus, we only need to average this term in order to the interface spacing,

$$\left\langle A^{\xi}_{jj'} \right\rangle_{\xi} = \left\langle e^{-iq\sum\limits_{k=j}^{j'-1}\xi_k} \right\rangle_{\xi} = \left\langle e^{-iq\sum\limits_{k=j}^{j'-1}(\bar{\xi}_k+\xi_k)} \right\rangle_{\xi} \tag{153}$$

This average is similar to the one already determined in the previous section for Δ_{jk}. So, we will apply the same procedure, transform the exponential of a summation into a product of exponentials,

$$\left\langle e^{-iq\sum\limits_{k=j}^{j'-1}(\bar{\xi}_k+\xi_k)} \right\rangle_{\xi} = \left\langle \prod_{k=j}^{j'-1} e^{-iq(\bar{\xi}_k+\xi_k)} \right\rangle_{\xi} \tag{154}$$

The interfaces are independent, as such, the average of the product becomes a product of averages,

$$\left\langle \prod_{k=j}^{j'-1} e^{-iq(\bar{\xi}_k+\xi_k)} \right\rangle_{\xi} = \prod_{k=j}^{j'-1} \left\langle e^{-iq(\bar{\xi}_k+\xi_k)} \right\rangle_{\xi} \tag{155}$$

These averages are similar to the ones determined in eq. (113). The average of each term of the product is given by eq. (103),

$$\begin{aligned} \left\langle e^{-iq(\bar{\xi}_k+\xi_k)} \right\rangle_{\xi} &= e^{-iq\bar{\xi}_k} \left\langle e^{-iq\xi_k} \right\rangle_{\xi} && (156) \\ &= e^{-q^2\sigma^2_{\xi j}/2+iq\bar{\xi}_k} && (157) \end{aligned}$$

, and the product is

$$\left\langle A^{\xi}_{jj'} \right\rangle_{\xi} = \prod_{k=j}^{j'-1} e^{-\beta^{\xi}_{k}} \tag{158}$$

, where

$$\beta^{\xi}_{k} \equiv \beta^{\xi}_{kr} + i\beta^{\xi}_{ki} \qquad \beta^{\xi}_{kr} \equiv q^2 \sigma^2_{\xi k}/2 \qquad \beta^{\xi}_{ki} \equiv q\bar{\xi}_k \tag{159}$$

With this, we can determine the average WAXS intensity for a multilayer with uncertainties in the atomic spacing and interface thickness.

4.4 LAYERS THICKNESS FLUCTUATION

There is still one last fluctuation from the perfect crystalline multilayer that we want to consider, a fluctuation in the thickness of the layers. The thickness of each layer, given by eq. (39), depends on both the number of atomic planes and the spacing between them. We already dealt with variations in the atomic spacing, so, we only need to address the fluctuations in the number of atomic planes N_j.

We allowed the spacing fluctuations to have any possible value. However, the layers must have a positive number of atomic planes. For this reason, its probability distribution needs to be restricted to the interval 0 to $+\infty$. Thus, we will use a single truncated Gaussian distribution to describe the number of atomic planes. This distribution is given by a standard Gaussian distribution divided by its own cumulative distribution in the truncation interval[109],

$$P(x) = \frac{e^{-(x-\bar{x})^2/2\sigma^2}}{\int\limits_{p}^{q} e^{-(x-\bar{x})^2/2\sigma^2}\, \mathrm{d}x} \tag{160}$$

Thus, the number of atomic planes follows the distribution,

$$P(N_j) = \frac{e^{-(N_j-\bar{N}_j)^2/2\sigma^2_{Nj}}}{\int\limits_{0}^{+\infty} e^{-(N_j-\bar{N}_j)^2/2\sigma^2_{Nj}}\, \mathrm{d}N_j} \tag{161}$$

Note that the $\bar{N}_j$ and N_j that appear in the truncated Gaussian distribution are not the real mean value and standard deviation values, they are defined for the standard distribution in the whole range. We need to compute $\langle\mu\rangle_N$ and $\langle\sigma\rangle_N$ to obtain the real values.

Fullerton[1, 111, 112] considers the number of atomic planes must be an integer and consequently a discrete distribution. Unlike him, we assume the atomic planes can be incomplete, and as such, they can have any real number and a continuous distribution.

The cumulative Gaussian distribution in eq. (161) is given by eq. (103),

$$\int_{0}^{+\infty} e^{-(N_j-\bar{N}_j)^2/2\sigma_{Nj}^2}\,\mathrm{d}N_j = \frac{\sqrt{2\pi\sigma_{Nj}^2}}{2}\left[\operatorname{erf}(+\infty) - \operatorname{erf}\left(\frac{-\bar{N}_j}{\sqrt{2\sigma_{Nj}^2}}\right)\right] \tag{162}$$

The error function has an asymptotic behaviour, $\lim_{x\to+\infty}=1$. Furthermore, the error function has an odd parity, thus, $\operatorname{erf}(-x)=-\operatorname{erf}(x)$. Using both, we obtain the cumulative distribution,

$$\int_{0}^{+\infty} e^{-(N_j-\bar{N}_j)^2/2\sigma_{Nj}^2}\,\mathrm{d}N_j = \frac{\sqrt{2\pi\sigma_{Nj}^2}}{2}\left[1 + \operatorname{erf}\left(\frac{\bar{N}_j}{\sqrt{2\sigma_{Nj}^2}}\right)\right] \tag{163}$$

Knowing the cumulative distribution, we get the probability distribution of the number of atomic planes,

$$P(N_j) = E_j e^{-(N_j-\bar{N}_j)^2/2\sigma_{Nj}^2} \tag{164}$$

, where

$$E_j \equiv \frac{2}{\sqrt{2\pi\sigma_{Nj}^2}}\frac{1}{1+\operatorname{erf}\left(\bar{N}_j/\sqrt{2\sigma_{Nj}^2}\right)} \tag{165}$$

Now that we have the probability distribution, we can continue with the determination of the average intensity. Once again, the averaging variables are independent, therefore, we can average the intensity separately over each one of them,

$$\langle I\rangle_{\Delta\xi N} = \left\langle P(\xi_j)P(N_j)P(\Delta_{jk})F_j'^{*}F_{j'}'\right\rangle \tag{166}$$

$$= \left\langle P(N_j)\langle I\rangle_{\Delta\xi}\right\rangle_N \tag{167}$$

The intensity averaged in relation to both the atomic spacing in the layers and the interfaces is given in eq. (81). Averaging it in relation to the number of atomic planes we obtain,

$$\langle I\rangle_{\Delta\xi N} = \sum_{j=1}^{N}\left\langle |F_j'|^2\right\rangle_N + 22\sum_{j=1}^{N-1}\sum_{j'>j}^{N}\Re\left[\left\langle A_{jj'}^{\xi}A_{jj'}^{\Delta}\right\rangle_N\right] \tag{168}$$

The term $A_{jj'}^{\xi}$ is given by eq. (158). This term does not depend on N_j. Thus, it is constant in the averaging integral of the crossed intensity. Therefore, in relation the crossed terms, we only need to average the terms $A_{jj'}^{\Delta}$. So, the average intensity becomes,

$$\langle I\rangle_{\Delta\xi N} = \sum_{j=1}^{N}\left\langle |F_j'|^2\right\rangle_{\Delta N} + 2\sum_{j=1}^{N-1}\sum_{j'>j}^{N}\Re\left[\left\langle A_{jj'}^{\xi}\right\rangle_{\xi}\left\langle A_{jj'}^{\Delta}\right\rangle_{\Delta N}\right] \tag{169}$$

Lets start by averaging the first terms, which correspond to the non-crossed intensity. These terms are given by eq. (127). Averaging them in order to the number of atomic planes we obtain,

$$\langle I_{nc}\rangle_{\Delta N} = \sum_{j=1}^{N} \left\langle |F_j'|^2 \right\rangle_{\Delta N} \tag{170}$$

$$= \sum_{j=1}^{N} \left|f_j\right|^2 \left\langle N_j + 2\Re\left[D_j\right]\right\rangle_N \tag{171}$$

$$= \sum_{j=1}^{N} \left|f_j\right|^2 \left[\left\langle N_j\right\rangle_N + 2\Re\left\langle D_j\right\rangle_N\right] \tag{172}$$

$$\tag{173}$$

, where

$$D_j \equiv \frac{N_j\left[e^{-\beta_j^{\Delta}} - e^{-2\beta_j^{\Delta}}\right] - e^{-\beta_j^{\Delta}} + e^{-(N_j+1)\beta_j^{\Delta}}}{\left[1 - e^{-\beta_j^{\Delta}}\right]^2} \tag{174}$$

The β_j^{Δ} term appears multiple times but does not depend on the number of atomic planes, as we can see from its definition in eq. (118). Thereby, only two terms in D_j depend on the number of planes and need to be averaged,

$$\left\langle D_j\right\rangle_N = \frac{\left\langle N_j\right\rangle_N\left[e^{-\beta_j^{\Delta}} - e^{-2\beta_j^{\Delta}}\right] - e^{-\beta_j^{\Delta}} + \left\langle e^{-(N_j+1)\beta_j^{\Delta}}\right\rangle_N}{\left[1 - e^{-\beta_j^{\Delta}}\right]^2} \tag{175}$$

The first average will give us the real mean value of the number of atomic planes,

$$\left\langle N_j\right\rangle_N = \int_0^{+\infty} N_j P(N_j)\,\mathrm{d}N_j \tag{176}$$

$$= E_j \int_0^{+\infty} N_j e^{-\left(N_j - \bar{N}_j\right)^2/2\sigma_{\bar{N}j}^2}\,\mathrm{d}N_j \tag{177}$$

We will start by changing the integration variable to $u \equiv N_j - \bar{N}_j$. With it the limits of integration will change to

$$0 < N_j < +\infty \tag{178}$$

$$-N_j < u < +\infty \tag{179}$$

With this, we can rewrite the integral in the new integration variable,

$$\left\langle N_j\right\rangle_N = E_j \int_{-N_j}^{+\infty} \left(u + \bar{N}_j\right) e^{-u^2/2\sigma_{\bar{N}j}^2}\,\mathrm{d}u \tag{180}$$

$$= E_j \int_{-N_j}^{+\infty} u e^{-u^2/2\sigma_{\bar{N}j}^2}\,\mathrm{d}u + \bar{N}_j E_j \int_{-N_j}^{+\infty} e^{-u^2/2\sigma_{\bar{N}j}^2}\,\mathrm{d}u \tag{181}$$

With the substitution, we obtained two integrals. The second is the integral of a truncated Gaussian distribution centred around zero. We can determine it using eq. (103),

$$\left\langle N_j \right\rangle_N = E_j \int_{-N_j}^{+\infty} u e^{-u^2/2\sigma_{Nj}^2} \,\mathrm{d}u + \bar{N}_j \tag{182}$$

The primitive of a exponential combined with a rational function, like in the first integral, is given by:[110, p. 109],

$$\int x^m e^{-ax^n} \,\mathrm{d}x = -\frac{e^{-ax^n}}{na} + const. \qquad \text{, for } \frac{m+1}{n} = 1 \tag{183}$$

With this, we can finish determining the mean number of atomic planes,

$$\left\langle N_j \right\rangle_N = \bar{N}_j - E_j\sigma_{Nj}^2 \left[e^{-\infty} - e^{-\bar{N}_j^2/2\sigma_{Nj}^2} \right] \tag{184}$$

$$= \bar{N}_j + E_j\sigma_{Nj}^2 e^{-\bar{N}_j^2/2\sigma_{Nj}^2} \tag{185}$$

The exponential Gaussian decays rapidly for large exponents. So, unless the standard deviation is close to the mean number of atomic planes,

$$\frac{\bar{N}_j}{E_j\sigma_{Nj}^2 e^{-\bar{N}_j^2/2\sigma_{Nj}^2}} \gg 1 \tag{186}$$

Although the real mean value is not the same as the one defined in the standard Gaussian distribution, the difference between them should be small, for reasonable standard deviation values. Furthermore, $|f_j|^2 \sum_{j=1}^{N} \left\langle N_j \right\rangle_N$ does not depend on scattering vector and consequently on the scattering angle, so it is a constant in the whole diffractogram. We will add a baseline and scale the final determined scattered intensity to reflect the measured intensities. Thus, this constant can safely be left out of the intensity's computation.

Now, we will determine the second average of D_j to obtain the average non-crossed intensity. The variable β_j^Δ does not depend on the number of layers, thus, we can move it outside the average integration,

$$\left\langle e^{-(N_j+1)\beta_j^\Delta} \right\rangle_N = e^{-\beta_j^\Delta} \left\langle e^{-N_j\beta_j^\Delta} \right\rangle_N \tag{187}$$

Averaging the exponential using the truncated Gaussian probability distribution from eq. (164),

$$\left\langle e^{-(N_j+1)\beta_j^\Delta} \right\rangle_N = e^{-\beta_j^\Delta} \int_0^{+\infty} P(N_j) e^{-N_j\beta_j^\Delta} \,\mathrm{d}N_j \tag{188}$$

$$= E_j e^{-\beta_j^\Delta} \int_0^{+\infty} e^{-(N_j-\bar{N}_j)^2/2\sigma_{Nj}^2} e^{-N_j\beta_j^\Delta} \,\mathrm{d}N_j \tag{189}$$

Expanding the factorized polynomial exponent inside the integral,

$$\left\langle e^{-(N_j+1)\beta_j^\Delta} \right\rangle_N = E_j e^{-\beta_j^\Delta} \int_0^{+\infty} e^{-\frac{N_j^2}{2\sigma_{Nj}^2} - 2N_j\left(\frac{\beta_j^\Delta}{2} - \frac{\bar{N}_j}{2\sigma_{Nj}^2}\right) - \frac{\bar{N}_j^2}{2\sigma_{Nj}^2}} \mathrm{d}N_j \tag{190}$$

We obtain the integral of an exponential with a second order polynomial exponent. The solution for this type of primitive integral can be found in integration tables[110, p. 109], see eq. (101),

$$\begin{aligned} \left\langle e^{-(N_j+1)\beta_j^\Delta} \right\rangle_N =& E_j e^{-\beta_j^\Delta} \frac{\sqrt{2\pi\sigma_{Nj}^2}}{2} e^{{\beta_j^\Delta}^2 \sigma_{Nj}^2/2 - \beta_j^\Delta \bar{N}_j} \\ & \times \left[\operatorname{erf}(+\infty) - \operatorname{erf}\left[\sqrt{2\sigma_{Nj}^2}\left(\frac{\beta_j^\Delta}{2} - \frac{\bar{N}_j}{2\sigma_{Nj}^2}\right)\right]\right] \end{aligned} \tag{191}$$

The error function with a complex argument, that has the real part larger than the imaginary part, presents an asymptotic behaviour similar to a error function with a real argument,

$$\lim_{\Re(z)\to+\infty} \operatorname{erf}(z) \approx 1 \tag{192}$$

The argument of the error function is:

$$\bar{N}_j - q^2\sigma_{\Delta j}^2\sigma_{Nj}^2/2 - iq\bar{d}_j\sigma_{Nj}^2 \tag{193}$$

, with this we can obtain the value of the first error function. The error function has an odd parity, thus, $\operatorname{erf}(-z) = -\operatorname{erf}(z)$, we will use this property to transform the second error function,

$$\begin{aligned} \left\langle e^{-(N_j+1)\beta_j^\Delta} \right\rangle_N =& E_j e^{-\beta_j^\Delta} \frac{\sqrt{2\pi\sigma_{Nj}^2}}{2} e^{{\beta_j^\Delta}^2 \sigma_{Nj}^2/2} e^{-\beta_j^\Delta \bar{N}_j} \\ & \times \left[1 + \operatorname{erf}\left(\frac{\bar{N}_j - \beta_j^\Delta \sigma_{Nj}^2}{\sqrt{2\sigma_{Nj}^2}}\right)\right] \end{aligned} \tag{194}$$

Finally, we combine the exponentials with the β_j^Δ exponent and replace the Gaussian normalisation constant E_j, defined in eq. (165),

$$\left\langle e^{-(N_j+1)\beta_j^\Delta} \right\rangle_N = e^{{\beta_j^\Delta}^2 \sigma_{Nj}^2/2 - \beta_j^\Delta(\bar{N}_j+1)} \frac{1 + \operatorname{erf}\left(\frac{\bar{N}_j - \beta_j^\Delta\sigma_{Nj}^2}{\sqrt{2\sigma_{Nj}^2}}\right)}{1 + \operatorname{erf}\left(\frac{\bar{N}_j}{\sqrt{2\sigma_{Nj}^2}}\right)} \tag{195}$$

Now, we only need to determine the crossed average intensity to obtain the final average total scattered intensity. The crossed intensity, defined in eq. (77), depends on two terms, $A_{jj'}^\xi$ and $A_{jj'}^\Delta$. The term $A_{jj'}^\xi$, defined in eq. (158), does not depend on the number of atomic planes in the layer, hence it does not need to be averaged. On the other hand, the term $A^{\Delta}_{jj'}$ depends on the number of atomic planes, thus, we only need to average the second term in relation to the number of atomic planes,

$$\langle I_c \rangle_{\Delta \xi N}(q) = 2 \sum_{j=1}^{N-1} \sum_{j'>j}^{N} \Re \left[\left\langle A^{\xi}_{jj'} \right\rangle_{\xi} \left\langle A^{\Delta}_{jj'} \right\rangle_{\Delta N} \right] \tag{196}$$

The $\left\langle A^{\Delta}_{jj'} \right\rangle_{\Delta}$ is given by eq. (149). The terms of this function depend on three different plane indices, j, j' and k. If we assume that each plane scatters the radiation independently from each other, we can determine three averages, one for the terms of each plane index,

$$\left\langle A^{\Delta}_{jj'} \right\rangle_{\Delta N} = J_j H_{j'} L_{jj'} \tag{197}$$

, where

$$J_j \equiv \left\langle F'^{*}_{j} e^{-iq\left[t_j + \sum_{r=1}^{N_j-1} \Delta_{jr}\right]} \right\rangle_{\Delta N} = \left\langle f^{*}_{j} \frac{e^{-(N_j-1)\beta^{\Delta}_{j}} - e^{+\beta^{\Delta}_{j}}}{1 - e^{+\beta^{\Delta}_{j}}} \right\rangle_{N} \tag{198}$$

$$H_{j'} \equiv \left\langle F'_{j'} \right\rangle_{\Delta N} = \left\langle f_{j'} \frac{1 - e^{-N_{j'}\beta^{\Delta}_{j'}}}{1 - e^{-\beta^{\Delta}_{j'}}} \right\rangle_{N} \tag{199}$$

$$L_{jj'} \equiv \left\langle e^{-iq \sum_{k>j}^{j'-1} \left[t_k + \sum_{r=1}^{N_k-1} \Delta_{kr}\right]} \right\rangle_{\Delta N} = \left\langle e^{-\sum_{k>j}^{j'-1} (N_k-1)\beta^{\Delta}_{k}} \right\rangle_{N} \tag{200}$$

We can transform $L_{jj'}$ in a product of exponentials,

$$L_{jj'} = \left\langle \prod_{k>j}^{j'-1} e^{-(N_k-1)\beta^{\Delta}_{k}} \right\rangle_{N} \tag{201}$$

In a kinematic model we assume that each atomic planes scatter the radiation independently from each other, thus, we can average each term separately,

$$L_{jj'} = \prod_{k>j}^{j'-1} \left\langle e^{-(N_k-1)\beta^{\Delta}_{k}} \right\rangle_{N} \tag{202}$$

The product terms are similar to an integral we already resolved in eq. (195), we can use that result to solve the averages,

$$L_{jj'} = \prod_{k>j}^{j'-1} e^{{\beta^{\Delta}_{k}}^2 \sigma^2_{Nk}/2} e^{-\beta^{\Delta}_{k}(\bar{N}_k-1)} \frac{1 + \operatorname{erf}\left(\frac{\bar{N}_k - \beta^{\Delta}_{k} \sigma^2_{Nk}}{\sqrt{2\sigma^2_{Nk}}} \right)}{1 + \operatorname{erf}\left(\frac{\bar{N}_k}{\sqrt{2\sigma^2_{Nk}}} \right)} \tag{203}$$

With this, we obtain the term of the k planes.

In $H_{j'}$, the exponential in the dividend is the only term that depends on the number of atomic planes and needs to be averaged,

$$H_{j'} = f_{j'} \frac{1 - \left\langle e^{-N_{j'}\beta^{\Delta}_{j'}} \right\rangle_N}{1 - e^{-\beta^{\Delta}_{j'}}} \tag{204}$$

The solution for this integral can by found in eq. (103),

$$\left\langle e^{-N_{j'}\beta^{\Delta}_{j'}} \right\rangle_N = e^{{\beta^{\Delta}_{j'}}^2 \sigma^2_{Nj'}/2} e^{-\beta^{\Delta}_{j'}\bar{N}} \frac{1 + \operatorname{erf}\left(\frac{\bar{N}_{j'} - \beta^{\Delta}_{j'}\sigma^2_{Nj'}}{\sqrt{2\sigma^2_{Nj'}}} \right)}{1 + \operatorname{erf}\left(\frac{\bar{N}_{j'}}{\sqrt{2\sigma^2_{Nj'}}} \right)} \tag{205}$$

In J_j, like in $H_{j'}$, only the exponential in the dividend with the N_j needs to be averaged,

$$J_j = f^*_j \frac{\left\langle e^{-(N_j-1)\beta^{\Delta}_j} \right\rangle_N - e^{+\beta^{\Delta}_j}}{1 - e^{+\beta^{\Delta}_j}} \tag{206}$$

This averaged is similar to the one we determined in $L_{jj'}$ just with a different index, j instead of k,

$$\left\langle e^{-(N_j-1)\beta^{\Delta}_j} \right\rangle_N = e^{{\beta^{\Delta}_j}^2 \sigma^2_{Nj}/2} e^{-\beta^{\Delta}_j(\bar{N}_j-1)} \frac{1 + \operatorname{erf}\left(\frac{\bar{N}_j - \beta^{\Delta}_j\sigma^2_{Nj}}{\sqrt{2\sigma^2_{Nj}}} \right)}{1 + \operatorname{erf}\left(\frac{\bar{N}_j}{\sqrt{2\sigma^2_{Nj}}} \right)} \tag{207}$$

4.5 FINAL FITTING EQUATION

We developed a kinematic model to describe WAXS spectra of multilayered thin films. The model is based on the structure factor with structural parameters that follow continuous Gaussian distributions. These parameters are the number of atomic planes and the distance between them. The model uses the following parameters to describe the WAXS intensity spectra:

f_j	layer's material average atomic scattering factor
$\bar{d}_j$	layer's average atomic spacing
$\sigma_{\Delta j}$	standard deviation of $\bar{d}_j$
$\bar{N}_j$	average number of atomic planes
σ_{Nj}	standard deviation of $\bar{N}_j$
$\bar{\xi}_j$	interface's average atomic spacing

$\sigma_{\xi j}$ standard deviation of $\bar{\xi}_j$

The model does not require information about the individual atomic planes, only of parameters' average values of each layer are required. The only information we need to know a priori is the average atomic scattering factor f_j of the different materials. The remaining parameters can be obtained directly from the XRD spectra.

According to the model, the average scattered X-ray intensity by a multilayer depends on two distinct terms,

$$\langle I \rangle_{\Delta \xi N} (q) = \langle I_{nc} \rangle_{\Delta N} + \langle I_c \rangle_{\Delta \xi N} \tag{208}$$

, for a scattering vector modulus

$$q = 4\pi \sin\theta / \lambda \tag{209}$$

, where θ is the X-ray scattering angle defined in fig. 2 and λ the wavelength of the incident radiation. The two terms are the non-crossed I_{nc} and crossed I_c intensities. The non-crossed intensity represents the scattering of each individual layers as if they were independent from the each other. While the crossed intensity represent the interference that occurs between the thin film layers.

The average non-crossed scattered X-ray intensity is defined as:

$$\langle I_{nc} \rangle_{\Delta \xi N} = \sum_{j=1}^{N} \left\langle |F'_j|^2 \right\rangle_{\Delta N} = \sum_{j=1}^{N} \left| f_j \right|^2 \left[\left\langle N_j \right\rangle_N + 2\Re \left\langle D_j \right\rangle_N \right] \tag{210}$$

$$\left\langle N_j \right\rangle_N = \bar{N}_j + \frac{2}{\sqrt{2\pi\sigma_{Nj}^2}} \frac{\sigma_{Nj}^2 e^{-\bar{N}_j^2/2\sigma_{Nj}^2}}{1 + \operatorname{erf}\left(\bar{N}_j / \sqrt{2\sigma_{Nj}^2} \right)} \tag{211}$$

$$\left\langle D_j \right\rangle_N = \frac{\left\langle N_j \right\rangle_N \left[e^{-\beta_j^\Delta} - e^{-2\beta_j^\Delta} \right] - e^{-\beta_j^\Delta} + e^{-\beta_j^\Delta} \left\langle e^{-N_j \beta_j^\Delta} \right\rangle_N}{\left[1 - e^{-\beta_j^\Delta} \right]^2} \tag{212}$$

$$\left\langle e^{-N_j \beta_j^\Delta} \right\rangle_N = e^{{\beta_j^\Delta}^2 \sigma_{Nj}^2 / 2 - \beta_j^\Delta \bar{N}_j} \frac{1 + \operatorname{erf}\left(\frac{\bar{N}_j - \beta_j^\Delta \sigma_{Nj}^2}{\sqrt{2\sigma_{Nj}^2}} \right)}{1 + \operatorname{erf}\left(\frac{\bar{N}_j}{\sqrt{2\sigma_{Nj}^2}} \right)} \tag{213}$$

$$\beta_j^\Delta \equiv q^2 \sigma_{\Delta j}^2 / 2 + iq\bar{d}_j \tag{214}$$

The second term, the crossed intensity, refers to the interference that happens in a multilayer and is defined as:

$$\langle I_c \rangle_{\Delta \xi N} = 2 \sum_{j=1}^{N-1} \sum_{j'>j}^{N} \Re \left[\left\langle A_{jj'}^{\xi} \right\rangle_{\xi} \left\langle A_{jj'}^{\Delta} \right\rangle_{\Delta N} \right] \tag{215}$$

$$\left\langle A^{\xi}_{jj'} \right\rangle_{\xi} = \prod_{k=j}^{j'-1} e^{-\left[q^2 \sigma_{\xi k}^2/2 + iq\bar{\xi}_k\right]} \tag{216}$$

$$\left\langle A^{\Delta}_{jj'} \right\rangle_{\Delta N} = J_j H_{j'} L_{jj'} \tag{217}$$

$$J_j = f_j^* \frac{e^{+\beta_j^{\Delta}} \left\langle e^{-N_j \beta_j^{\Delta}} \right\rangle_N - e^{+\beta_j^{\Delta}}}{1 - e^{+\beta_j^{\Delta}}} \tag{218}$$

$$H_{j'} = f_{j'} \frac{1 - \left\langle e^{-N_{j'} \beta_{j'}^{\Delta}} \right\rangle_N}{1 - e^{-\beta_{j'}^{\Delta}}} \tag{219}$$

$$L_{jj'} = \prod_{k>j}^{j'-1} e^{\beta_k^{\Delta}} \left\langle e^{-N_k \beta_k^{\Delta}} \right\rangle_N \tag{220}$$

This crossed intensity only occurs if the thin film has more than one layer and is the only term that depends on the interface between layers. Unlike the non-crossed intensity, it depends on the indices of two layers, j and j', because it deals with the interference.

4.6 FITTING

Now that we have a model that describes the WAXS spectra of thin film multilayers, we will use it to obtain information about the structure of our BSL samples. The model should allow us to determine the structural parameters described in section 4.5, as well as, give an idea of the amount of disorder in those parameters.

An understanding of how each parameter affects the model spectra makes it easier to choose the initial fitting parameters. For this reason, we will determine the behaviour of each parameter has in the spectra.

The atomic scattering factor f_j depends on the type of material, the energy of the incident radiation and the scattering vector. Our model considers the incident radiation has constant energy. We will analyse small angle range, in this case, the scattering factor should not change much, as such, we will treat f_j as constant in that region. In that case, the f_j acts as a scaling factor for the relative reflectivity associated with different materials.

The interface's average atomic spacing $\bar{\xi}_j$ only appears in eq. (216). They act as a phase that shifts each term of the crossed intensities in the scattering vector, and consequently in the scattering angle. The standard deviation $\sigma_{\xi j}$ also only appears in eq. (216).

The effect of the remaining parameters is complicated to access, so, to more easily understand their effect of the individual parameters, we will simulate WAXS spectra using the obtained model. In fig. 25, we present the result of these simulations.

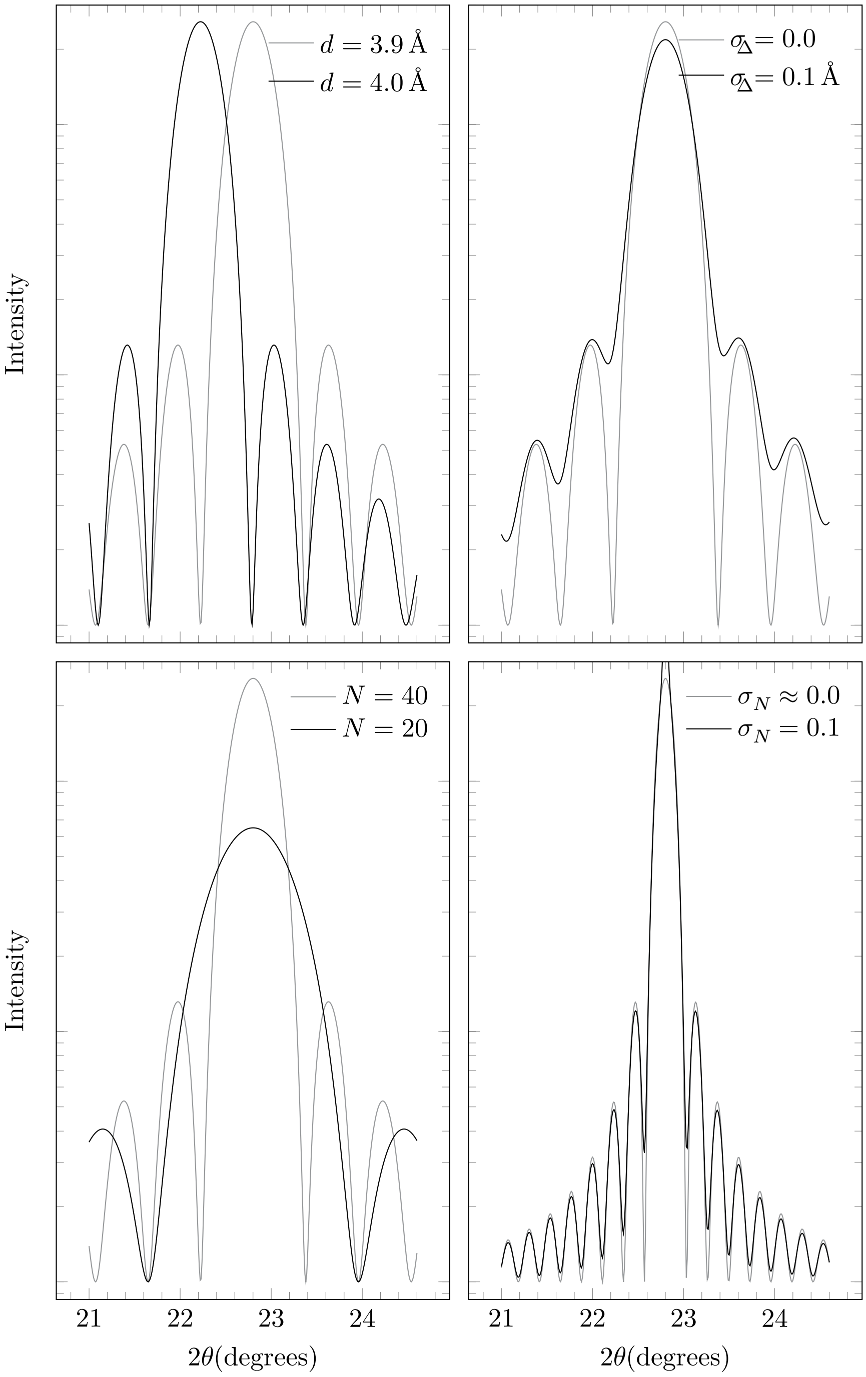

Figure 25: Effect of the variation of the number of atomic planes (a), its standard deviation (b), the spacing between them and (c) the standard deviation of the spacing (d) in WAXS spectra. The results were obtained by simulation a single layer of STO with the developed WAXS model, in the region of the [100] diffraction peak.

As expected from Bragg's Law, the atomic spacing is responsible for the scattering angle of the first order peak. As we can observe from the simulation, both N_j and $\sigma_{\xi j}$ have an inverse relation with the maximum scattered amplitude. Furthermore, we will need to apply a scaling factor to the spectra obtained by the model to correctly represent the data. The number of atomic planes also has an inverse relation with the peaks' full width at half maximum (FWHM) and the angular period between the satellites peaks. On the other hand, the $\sigma_{\xi j}$ is related to the level of disorder the lattice has, and as expected, it reduces the amplitude of all peaks, not just the central peak like the number of layers and softens the tail of peak. The satellite peaks can disappear in the peak's tail if $\sigma_{\xi j}$ is high enough.

A simulation of the effect of its standard deviation can be seen in fig. 26.

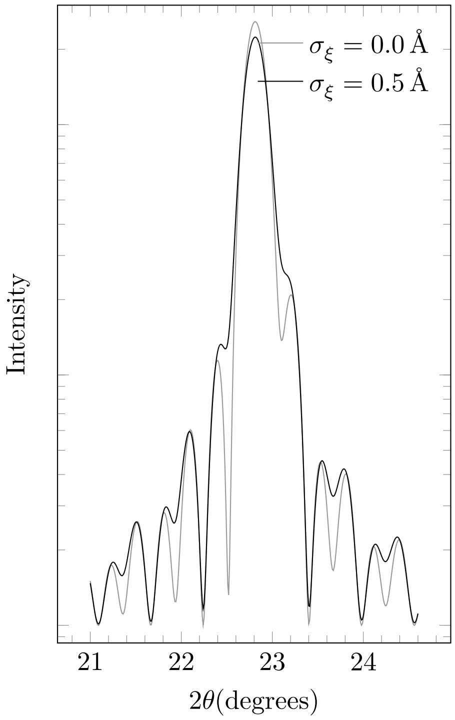

Figure 26: Effect of variation of the interface spacing standard deviation in the WAXS spectra of a multilayer STO\LSMO structure.

In addition to the parameters needed by the model, we also require a scaling factor and a baseline to more precisely describe the measured spectra that are in arbitrary units. The scattering angle range we will analyse is small, as such, a constant baseline should suffice. The model has the term $|f_j|^2 \sum_{j=1}^{N} \langle N_j \rangle$, seen in eq. (210). This term is constant and can be ignored because it becomes inconsequential with the added constant baseline. The scaling factor aggregates, among others, the power of the diffractometer and the area of the sample that was irradiated.

These two alter the intensity of the spectra independently of the studied sample.

Other techniques can determine all parameters required by the model; however, this is not necessary. Except for the atomic scattering powers, we will rely solely on the information provided by the WAXS spectra to determine the structural information of the samples.

We already determined some of those parameters in the SAXS analysis on section 3.5. Among them are the scattering powers of the different layers present in table 4. As we did in the SAXS analysis, we will consider that the scattering powers are constant and they will not fluctuate during the fitting procedure. Although the atomic scattering power depends on the scattering vector, we will fit only small scattering angle ranges; therefore, the atomic scattering power is almost constant in the region.

When it comes to the atomic spacing, we determined its values for the ideal monocrystals, see table 2. These values will change due to structural disorder, caused for example by lattice mismatch that leads to strain. In case the centre most intense peak is visible, we can use Bragg's Law from eq. (1), to determine the average spacing. However, the peaks are not always visible, especially if the layers have low thickness. For the number of atomic planes N_j, we will start with the expected values in table 3, that were obtained taking into account the condition of deposition. However, for the values were already determined by SAXS, and as such, for peaks that are not visible we will start with those values instead, that should be closer to the real values.

The WAXS analyses were performed in a θ–2θ configuration. As seen in section 1.1.1, with this configuration we can only see the planes that are perpendicular to the film's surface. All layers of the samples have a perovskite structure that has grown in a [100] direction on top of a substrate with the same direction and structure. The layers were grown through PLD that assures high crystallinity. Thus, we can expect to detect the (n00) planes from all layers. We will analyse the peaks of the (100) planes, that should have scatterings angles 2θ around 22°, as seen in table 2.

The model provides a formula to describe the WAXS spectra of multilayers that can be extensive for multilayers with several layers. Not only is the formula extensive but there are also several parameters that need to be adjusted. The number of parameters is proportional to the number of layers, with $6N$ parameters that need to be fitted if we take the baseline and scaling factor into account and consider the atomic form factor to be constant. So, for the samples with three layers that we will analyse, a total of 18 parameters need to be adjusted. Furthermore, some of those parameters have similar influences in the spectra, as seen in fig. 25, and the diffractograms do not present satellite peaks, making it difficult to access the parameter's real values. For these reasons, we developed software to perform the fit of WAXS diffractogram with the developed model. The software resorts to a pre-existing solver provided by the C++ library *Ceres Solver*[113]. This solver is an implementation of the Levenberg-Marquardt algorithm[102, 103], using an exact step[114]. This algorithm is an optimisation algorithm that we will use to find the residues' local minima.

The X-ray beam penetrates the samples up to a depth that is proportional to the $\sin\theta$ and depends on the penetrated material. For SAXS, the penetration depth is, usually, in the order of the tens of micrometer[3, 15, 16]. The thin films from our samples should have thicknesses at least an order of magnitude below the X-ray penetration depth. Consequently, the substrate will be the largest contributor to the scattered intensity. As seen in section 1.2, the layers should have scattering angles that are close to the substrate angle unless there is significant disorder to shift the angles. So, the peaks from the layers can be enveloped, at least partially, in the much more intense substrate's peak. In the case of the intermediate layer of STO, its contribution to the STO peak should be negligible, as such, the fitting of this peak will be unreliable.

The substrate will be responsible for a significant modulation of the scattered X-ray and needs to be taken into account. To represent the substrate contribution to the samples' spectra, we used a WAXS spectrum of a STO substrate, see fig. 27. This spectrum was shifted and scaled to better represent the substrate contribution in the spectra of our samples and used as a baseline in the fitting procedure.

Although the scattering angle of the thin film layers will change from the bulk materials, they have close lattice constants, so, the difference should be small. The first order of scattering peaks should occur around 22.5°, as seen in section 1.2. As such, we used the developed model to analyse the WAXS spectra in the region from 21 to 26°, see fig. 28 on pages 70 to 71.

As discussed in section 1.1.2, the incident X-ray radiation has several wavelengths. However, structural disorder broadens the peaks. Only the substrate has sufficiently high crystallinity to display a discernible peaks' doublet from the CuK$\bar{\alpha}$ radiation. For this reason, we only considered the CuK$\bar{\alpha}$ radiation in our analysis with a wavelength of 1.541 84 Å.

The samples' WAXS spectra do not display satellite peaks. As we saw in section 4.5, on page 62, the absence of satellite peaks indicates a high amount of disorder in samples' crystalline structure. Therefore, we expect to obtain high standard deviation values for the structural parameters. Without satellite peaks, we can rely on their scattering angle to determine with accuracy the number of atomic planes. We need to depend on the peaks' intensity to determine the number of atomic planes. Several parameters affect the intensity, because of that, the results obtained this way will not be as reliable as it could be

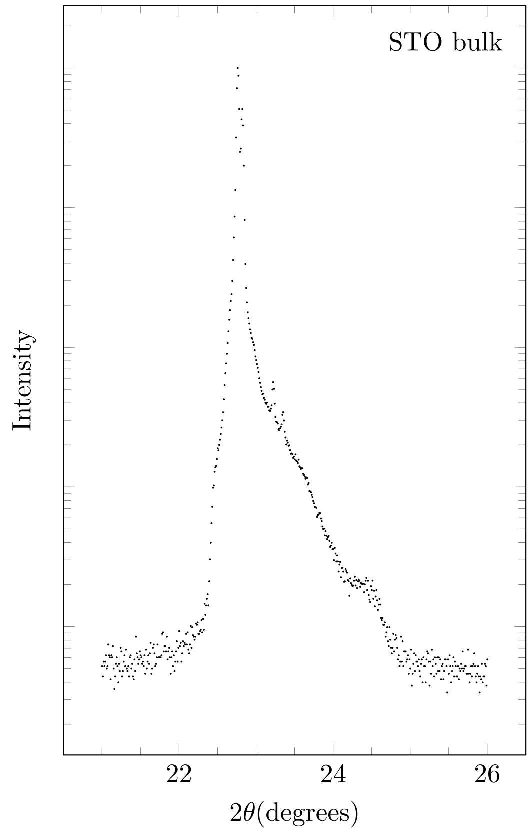

Figure 27: WAXS diffractogram of bulk $SrTiO_3$ like the substrates used in the BSL samples.

with the presence of satellite peaks. Furthermore, the STO peaks are completely and the BLFO partly engulfed by the substrate peak. Thus, we will rely mainly on thicknesses obtained by SAXS for those peaks. The fits performed on the spectra are in fig. 28.

In table 7, we present the structural parameters obtained by the fits. In table 8, on page 72, we have the expected thicknesses, as well as, the ones obtained by SAXS and WAXS.

A comparison between the expected (t_E) and fitted thicknesses (t_f) indicate a drift in the calibration of the deposition time with increasing sample deposition (sample number), due to increased target use. The calculated total roughness, defined by:

$$\sigma_t = \sqrt{\sigma_{\Delta j}^2 + \left(\bar{d}_j \sigma_{Nj}\right)^2 + \sigma_{\xi j}^2} \tag{221}$$

is around 1 Å, see table 7, and similar in the different samples indicating similar growth conditions. The values are near from the corresponding fitted SAXS ones.

There are also discrepancies between the thicknesses obtained by SAXS and WAXS. In SAXS, the frequency of the fringes in the spectra is proportional to the thickness. If the thickness is high enough, the fringe becomes smaller than the measurement equipment resolution. In those cases, the obtained thickness values are less precise.

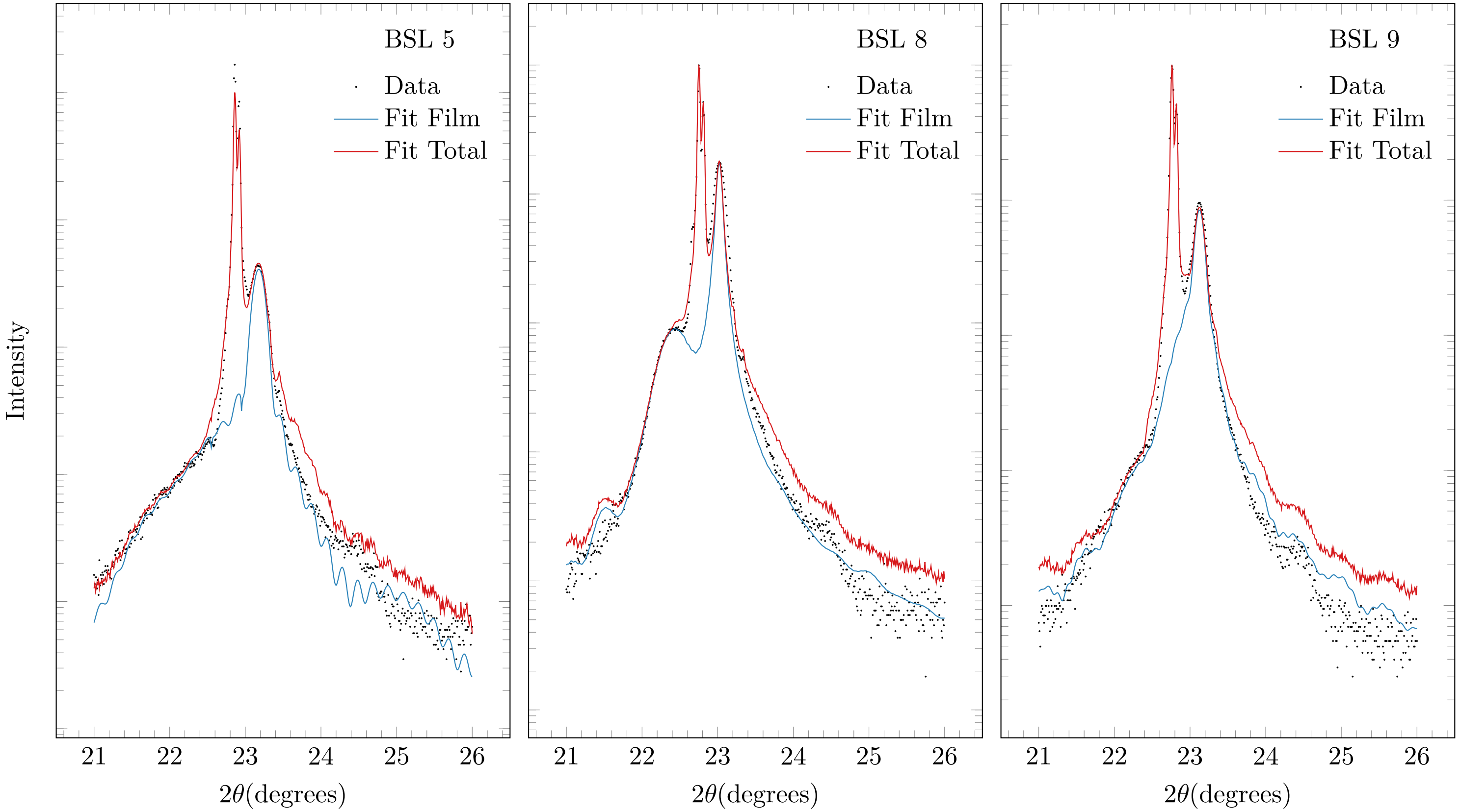
Intensity
BSL 5
Data
Fit Film
Fit Total
BSL 8
Data
Fit Film
Fit Total
BSL 9
Data
Fit Film
Fit Total
21
22
23
24
25
26
2θ(degrees)

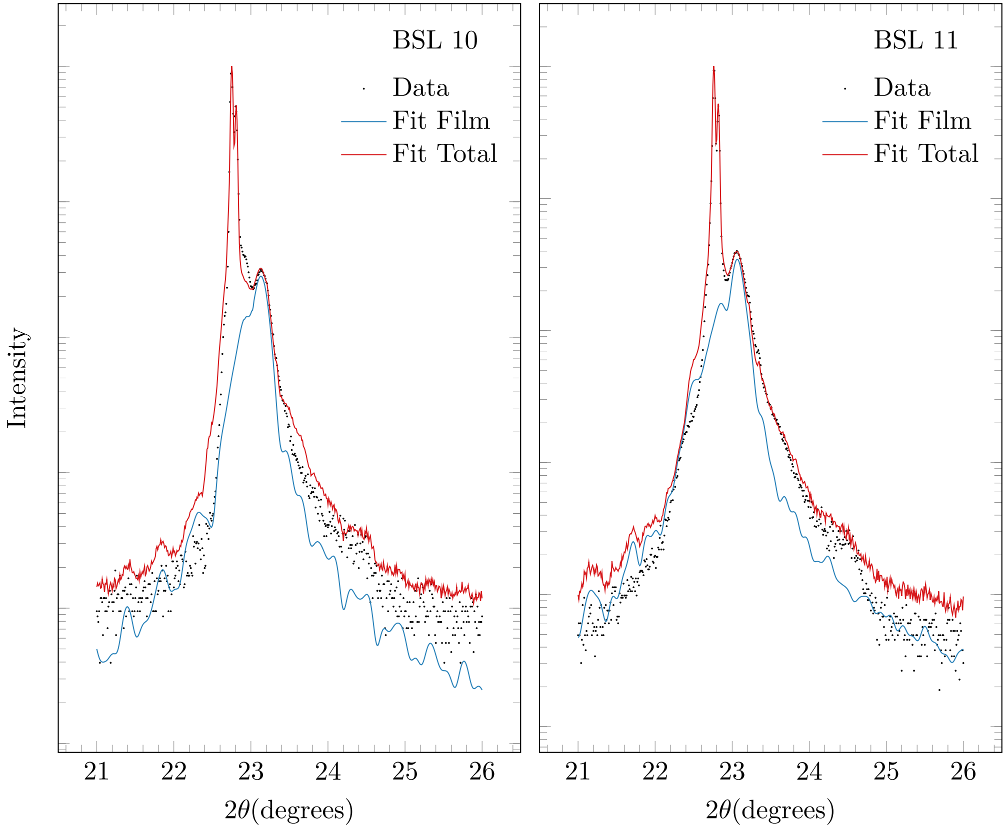

Figure 28: Fitted WAXS spectra of the BSL samples.

Table 7: Structural parameter values of the BSL samples obtained by WAXS measurements fitted with the developed WAXS model.

Sample	Layer	$\bar{d}_j$(Å)	$\sigma_{\Delta j}$(Å)	$\bar{N}_j$	σ_{Nj}	$\bar{\xi}_j$(Å)	$\sigma_{\xi j}$(Å)	σ_t(Å)
BSL 5	LSMO	3.837	0.062	117	0.006	3.813	1.198	1.637
	STO	3.875	0.051	17	0.010	3.937	1.109	
	BLFO	3.943	0.068	13	0.007	—	—	
BSL 8	LSMO	3.863	0.078	370	0.016	3.903	0.530	0.878
	STO	3.935	0.077	19	0.011	3.956	0.680	
	BLFO	3.974	0.091	39	0.008	—	—	
BSL 9	LSMO	3.845	0.074	180	0.017	3.894	0.908	1.453
	STO	3.908	0.069	18	0.011	3.891	1.121	
	BLFO	3.865	0.102	41	0.013	—	—	
BSL 10	LSMO	3.840	0.061	113	0.009	3.854	0.947	1.310
	STO	3.863	0.053	43	0.016	3.878	0.896	
	BLFO	3.880	0.058	53	0.007	—	—	
BSL 11	LSMO	3.849	0.083	115	0.011	3.867	0.496	0.792
	STO	3.877	0.076	53	0.013	3.893	0.598	
	BLFO	3.919	0.077	38	0.008	—	—	

Table 8: Thicknesses expected t_E and obtained by SAXS t_S and WAXS t_W for the layers of the characterized BSL samples.

Sample	Layer	t_E(nm)	t_S(nm)	t_W(nm)
BSL 5	LSMO	10	45.16	44.51
	STO	5	7.38	6.20
	BLFO	5	4.36	4.73
BSL 8	LSMO	20	86.80	142.54
	STO	5	9.97	7.08
	BLFO	80	20.72	15.10
BSL 9	LSMO	20	38.60	68.83
	STO	7.5	16.25	6.64
	BLFO	20	22.78	15.46
BSL 10	LSMO	20	43.25	43.01
	STO	15	17.21	16.22
	BLFO	40	20.56	20.18
BSL 11	LSMO	20	120.13	43.88
	STO	22.5	17.67	20.16
	BLFO	40	46.57	14.50

A good SAXS fit relies heavily on the presence of visible fringes, without them the fitting is more difficult. Samples BSL 5 and 10 have well-discerned fringes, and as such, give confidence in the SAXS results obtain from these two samples. Although with only a slight “bump” in the spectrum, giving a higher error, the fit of the sample BSL 8 is also is consistent with the observed trend.

The WAXS spectra also allow better thickness results if they have visible fringes. Unlike SAXS it is still possible to determine the thicknesses if the peak is visible. In all samples, the STO layer is entirely engulfed by the substrate peak, and as such, the obtained results for these layers have higher uncertainty.

Comparing the results for the LSMO and BLFO layers, it is observed that the the ones obtained from SAXS and WAXS are similar for samples BSL 5 and 10 and also for sample BSL 8. For samples BSL 9 and 11 the WAXS is more reliable due to their featureless SAXS spectra.

5

CONCLUSION

We developed a model and fitting software to describe the WAXS spectra of multilayered thin films. This model allowed us to quantify the structural information and disorder of the individual layers, more concretely the atomic spacing, number of atomic planes and the thickness of the interfaces. For comparison, we also analysed the SAXS spectra of our samples with an already existing model that provides the thickness and the atomic density of the layers, as well as the roughness of surfaces and interfaces.

For our thicker samples, the developed WAXS model was more reliable than the SAXS to determine the structural information. With our model, we can also determine the amount of structural disorder, unlike the used SAXS model. However, we should not disregard the SAXS as it can complement the WAXS results in thinner samples. With SAXS we can obtain the structural information of peaks masked by larger peaks, like the peaks created by the substrate in the case of our samples.

We were only able to compare with certainty the thicknesses determined from both techniques in three of our samples, but in those the values are close. A comparison with the expected deposition values indicates a drift of the calibration of deposition times and the need for a post-deposition analysis to determine the actual thickness of the layers and samples.

5.1 SUGGESTION OF FUTURE WORKS

More directed techniques like scanning electron microscope (SEM) and transmission electron microscopy (TEM) could allow an improved comparison with the obtained results. The software could also be improved to compute an estimation of the statistical standard deviation of obtained parameters and the goodness of the fits. The model could also be improved with the inclusion of strain gradients originated from the mechanical coupling at the interfaces between the different layers or with the use of different roughness profiles (e.g., additive roughness). The possibility of intermixing could also be taken into account by allowing the variation of the atomic scattering factors along the interfacial region. Nevertheless, due to the increased number of fitting parameters in these cases, complementary techniques for structural and chemical properties of the films would be important to determine relevant parameters, prior to the fitting procedure.

BIBLIOGRAPHY

[1] Eric E. Fullerton et al. 'Structural refinement of superlattices from x-ray diffraction'. In: *Physical Review B* 45.16 (1992), pp. 9292–9310.

[2] Yifei Meng et al. 'Digital model for X-ray diffraction with application to composition and strain determination in strained InAs/GaSb superlattices'. In: *Journal of Applied Physics* 116.1 (July 2014), p. 013513.

[3] René Guinebretière. *X-ray diffraction by polycrystalline materials.* John Wiley & Sons, 2013.

[4] Jean Daillant and Alain Gibaud. *X-ray and neutron reflectivity: principles and applications.* Daillant, vol. 770. Springer Berlin Heidelberg, 2009, pp. 87–120.

[5] N David Mermin Neil W.(Neil W. Ashcroft) Ashcroft. *Solid state physics.* 1st ed. Solid State Physics. Holt, Rinehart and Winston, 1976.

[6] F de Bergevin. 'The Interaction of X-Rays (and Neutrons) with Matter'. In: *X-ray and Neutron Reflectivity.* Springer, 2009, pp. 1–57.

[7] Isabel Alexandra Domingues Tarroso Gomes. 'Manganite thin films deposited on piezoelectric substrates'. Ph.D. Thesis. Universidade do Minho, 2013.

[8] J. A. Bearden. 'X-ray wavelengths'. In: *Reviews of Modern Physics* 39.1 (1967), pp. 78–124.

[9] H. Berger. 'Study of the Kalpha emission spectrum of copper'. In: *X-Ray Spectrometry* 15.4 (1986), pp. 241–243.

[10] G. Hölzer et al. 'K a1,2 and K b1,3 x-ray emission lines of the 3d transition metals'. In: *Physical Review A* 56.6 (1997), pp. 4554–4568.

[11] E. Prince. *International Tables for Crystallography, Mathematical, Physical and Chemical Tables.* 3rd. Vol. volume C. IUCr Series. International Tables of Crystallography. Wiley, 2004.

[12] M. Deutsch et al. 'X-ray spectrometry of copper: New results on an old subject'. In: *Journal of Research of the National Institute of Standards and Technology* 109.1 (Jan. 2004), p. 75.

[13] R D Deslattes et al. 'X-ray transition enerfies new approach to a comprehensive evaluation.pdf'. In: *Reviews of Modern Physics* 75.1 (Jan. 2003), pp. 35–99.

[14] RFNC VNIITF and JIHT RAS. *Spectr-W^3 Database on Spectroscopic Properties of Atoms and Ions@ONLINE.* URL: `http://spectr-w3.snz.ru/index.phtml`.

[15] Tom Ryan. 'The Development of Instrumentation for Thin-Film X-ray Diffraction'. In: *Journal of Chemical Education* 78.5 (2001), pp. 613–616.

[16] A Gibaud and Guillaume Vignaud. 'Specular reflectivity from smooth and rough surfaces'. In: *X-ray and Neutron Reflectivity.* Springer, 2009, pp. 85–131.

[17] B E Warren. *X-ray Diffraction, reprint.* 1990.

[18] Andrei Benediktovitch, Ilya Feranchuk and Alexander Ulyanenkov. *Theoretical concepts of x-ray nanoscale analysis.* Springer, 2014.

[19] Boris W Batterman and Henderson Cole. 'Dynamical diffraction of x rays by perfect crystals'. In: *Reviews of modern physics* 36.3 (1964), p. 681.

[20] André Authier. *Dynamical theory of X-ray diffraction.* Springer, 2006.

[21] Ullrich Pietsch, Vaclav Holy and Tilo Baumbach. *High-resolution X-ray scattering: from thin films to lateral nanostructures.* Springer Science & Business Media, 2013.

[22] Y S Gu et al. 'Structural studies of Fe/Pd magnetic multilayers by x-ray diffraction'. In: *Physical Review B* 50.9 (1994), p. 6119.

[23] Vasily I. Punegov, Sergey I. Kolosov and Konstantin M. Pavlov. 'Darwin's approach to X-ray diffraction on lateral crystalline structures'. In: *Acta Crystallographica Section A: Foundations and Advances* 70.1 (2014), pp. 64–71.

[24] Shuai Dong et al. 'Multiferroic materials and magnetoelectric physics: symmetry, entanglement, excitation, and topology'. In: (2015).

[25] Hans Schmid. 'Multi-ferroic magnetoelectrics'. In: *Ferroelectrics* 162.1 (1994), pp. 317–338.

[26] N. A. Spaldin. 'MATERIALS SCIENCE: The Renaissance of Magnetoelectric Multiferroics'. In: *Science* 309.5733 (2005), pp. 391–392.

[27] Matthias Opel. 'Spintronic oxides grown by laser-MBE'. In: *Journal of Physics D: Applied Physics* 45.3 (2011), p. 33001.

[28] José Manuel Gusman Correia Araújo and Barbosa. 'Nano-estruturas Compósitas Multiferroicas'. Ph.D. Thesis. Universidade do Minho, 2013.

[29] Fumihiro Matsukura, Yoshinori Tokura and Hideo Ohno. 'Control of magnetism by electric fields'. In: *Nature Nanotechnology* (2015).

[30] Heng Wu et al. *Recent progress on the structural characterizations of domain structures in ferroic and multiferroic perovskite oxides: A review.* 2015.

[31] Melvin M. Vopson. 'Fundamentals of Multiferroic Materials and Their Possible Applications'. In: *Critical Reviews in Solid State and Materials Sciences* 40.4 (2015).

[32] L. W. Martin et al. 'Multiferroics and magnetoelectrics: thin-films and nanostructures'. In: *Journal of Physics C* 20.43 (2008), 434220 (13pp).

[33] L.W. Martin, Y.-H Chu and R. Ramesh. '2010-Advances in the growth and characterization of magnetic, ferroelectric, and multiferroic oxide thin films'. In: *Materials Science and Engineering* 68.4-6 (2010), pp. 89–133.

[34] Wilma Eerenstein et al. 'Scott: Multiferroic and magnetoelectric materials'. In: *Nature* 442759 (2006), pp. 759–765.

[35] Manuel Bibes, Javier E. Villegas and Agnès Barthélémy. 'Ultrathin oxide films and interfaces for electronics and spintronics'. In: *Advances in Physics* 60.1 (2011), pp. 5–84.

[36] Manfred Fiebig. 'Revival of the magnetoelectric effect'. In: *Journal of Physics D: Applied Physics* 38.8 (2005), R123–R152.

[37] Ce Wen Nan et al. 'Multiferroic magnetoelectric composites: Historical perspective, status, and future directions'. In: *Journal of Applied Physics* 103.3 (2008).

[38] Jing Ma et al. 'Recent progress in multiferroic magnetoelectric composites: From bulk to thin films'. In: *Advanced Materials* 23.9 (Mar. 2011), pp. 1062–1087.

[39] James F Scott. 'Applications of magnetoelectrics'. In: *Journal of Materials Chemistry* 22.11 (2012), p. 4567.

[40] K F Wang, J. -M. Liu and Z F Ren. 'Multiferroicity: The coupling between magnetic and polarization orders'. In: *Advances in Physics* (2009).

[41] Julia A. Mundy et al. 'Atomically engineered ferroic layers yield a room-temperature magnetoelectric multiferroic'. In: *Nature* 537.7621 (2016), pp. 523–527.

[42] C. H. Ahn, K. M. Rabe and J.-M. J-M Triscone. 'Ferroelectricity at the Nanoscale: Local Polarization in Oxide Thin Films and Heterostructures'. In: *Science* 303.5657 (Jan. 2004), pp. 488–491.

[43] Martin Gajek et al. 'Tunnel junctions with multiferroic barriers.' In: *Nature materials* 6.4 (2007), pp. 296–302.

[44] Teresa Maria Tranchete de Carvalho. 'Síntese e caracterização de materiais cerâmicos e filmes finos multiferróicos para aplicação em sensores e atuadores'. Ph.D. Thesis. Universidade de Trás-os-Montes e Alto Douro, 2012.

[45] Albert Fert. ‘Origin, development, and future of spintronics (Nobel lecture)’. In: *Angewandte Chemie - International Edition*. Vol. 47. 32. July 2008, pp. 5956–5967.

[46] Biplab Pal, Rudolf A. Römer and Arunava Chakrabarti. ‘Spin filter for arbitrary spins by substrate engineering’. In: *Journal of Physics: Condensed Matter* 28.33 (Apr. 2016), p. 12.

[47] Guo-Xing Miao, Martina Müller and Jagadeesh Moodera. ‘Magnetoresistance in Double Spin Filter Tunnel Junctions with Nonmagnetic Electrodes and its Unconventional Bias Dependence’. In: *Physical Review Letters* 102.7 (2009), pp. 1–4.

[48] Gertjan Koster, Mark Huijben and Guus Rijnders. *Epitaxial Growth of Complex Metal Oxides*. Elsevier, 2015.

[49] Stephan Borek et al. ‘Multiferroic heterostructures for spin filter applications: An \textit{ab initio} study’. In: *Phys. Rev. B* 92.17 (Nov. 2015), p. 174408.

[50] George T. Rado. ‘Observation and possible mechanisms of magnetoelectric effects in a ferromagnet’. In: *Physical Review Letters* 13.10 (1964), pp. 335–337.

[51] J Wang et al. ‘Epitaxial $BiFeO_3$ multiferroic thin film heterostructures.’ In: *Science (New York, N.Y.)* 299.5613 (2003), pp. 1719–1722.

[52] James F Scott. ‘Room-temperature multiferroic magnetoelectrics’. In: *NPG Asia Materials* 5.11 (Nov. 2013), e72.

[53] Alexander Frank Wells. *Structural Inorganic Chemistry*. 4th ed. Clarendon, 1975, pp. 483–487.

[54] H Kronmüller and S Parkin. *Handbook of magnetism and advanced magnetic materials: Spintronics and magnetoelectronics*. Handbook of Magnetism and Advanced Magnetic Materials. John Wiley & Sons, 2007.

[55] Y. Tokura. ‘Fundamental Features of Colossal Magnetoresistive Manganese Oxides’. In: *Colossal Magnetoresistive Oxides* (2000), p. 1.52.

[56] J. M. D. Coey, M. Viret and S. von Molnár. ‘Mixed-valence manganites’. In: *Advances in Physics* 48.2 (1999), pp. 167–293.

[57] G.H. Jonker and J.H. Van Santen. ‘Ferromagnetic compounds of manganese with perovskite structure’. In: *Physica* 16.3 (1950), pp. 337–349.

[58] A-M Haghiri-Gosnet and J-P Renard. ‘CMR manganites: physics, thin films and devices’. In: *Journal of Physics D: Applied Physics* 36.8 (2003), R127–R150.

[59] Ulrich Müller. *Inorganic Structural Chemistry*. Second edi. 2006.

[60] Ana Claúdia Lourenço Santana Marques. ‘Advanced Si pad detector development and $SrTiO_3$ studies by emission channeling and hyperfine interaction experiments’. Ph.D. Thesis. Universidade de Lisboa, 2009, pp. 11–31.

[61] Chonghe Li, Kitty Chi Kwan Soh and Ping Wu. ‘Formability of ABO3 perovskites’. In: *Journal of Alloys and Compounds* 372.1-2 (2004), pp. 40–48.

[62] Mats Johnsson and Peter Lemmens. ‘Crystallography and Chemistry of Perovskites’. In: *John Wiley & Sons, Ltd., New York* (2007), p. 11.

[63] A P Ramirez. ‘Colossal magnetoresistance’. In: *Journal Of Physics-Condensed Matter* 9.39 (1997), pp. 8171–8199.

[64] M.-J. Casanove et al. ‘Growth and relaxation mechanisms in La0.66Sr0.33MnO3 manganites deposited on SrTiO3(001) and MgO(001)’. In: *Applied Surface Science* 188.1-2 (2002), pp. 19–23.

[65] P. M. Woodward. ‘Octahedral Tilting in Perovskites. II. Structure Stabilizing Forces’. In: *Acta Crystallographica B* 53.1 (1997), pp. 44–66.

[66] Karin M Rabe et al. ‘Modern Physics of Ferroelectrics: Essential Background’. In: *Physics of Ferroelectrics: A Modern Perspective.* Berlin, Heidelberg: Springer Berlin Heidelberg, 2007, pp. 1–30.

[67] R. Seshadri and N. A. Hill. ‘Visualizing the role of Bi 6s ”lone pairs” in the off-center distortion in ferromagnetic BiMnO3’. In: *Chemistry of Materials* 13.9 (2001), pp. 2892–2899.

[68] N Kallel et al. ‘Structure, magnetic and electrical behaviour of $La_{0.7}Sr_{0.3}Mn_{1-x}Ti_xO_3$ with 0<x<0.3’. In: *Journal of Magnetism and Magnetic Materials* 261.1-2 (2003), pp. 56–65.

[69] R Cherif et al. ‘Structural, magnetic and magnetocaloric properties of $La_{0.7}Sr_{0.3}MnO_3$ manganite oxide prepared by the ball milling method’. In: *European Physical Journal Plus* 129 (2014), p. 83.

[70] E Vescovo et al. ‘Direct evidence for a half-metallic ferromagnet’. In: *Nature* 392.April (1998), pp. 794–796.

[71] Arturas Vailionis et al. ‘Anisotropic stress relief mechanism in epitaxial $La_{0.67}Sr_{0.33}MnO_3$ films’. In: *Applied Physics Letters* 95.2009 (2009), p. 152508.

[72] ‘$SrTiO_3$ crystal structure, lattice parameters’. In: *Ternary Compounds, Organic Semiconductors.* Ed. by O Madelung, U Rössler and M Schulz. Berlin, Heidelberg: Springer Berlin Heidelberg, 2000, pp. 1–3.

[73] Gustau Catalan and James F. Scott. ‘Physics and applications of bismuth ferrite’. In: *Advanced Materials* 21.24 (June 2009), pp. 2463–2485.

[74] V. R. Palkar et al. ‘Magnetoelectricity at room temperature in $\mathrm{Bi_{0.9\text{-}x}Tb_xLa_{0.1}FeO_3}$ system’. In: *Phys. Rev. B* 69 (2004), p. 11.

[75] D K Fork, D B Chrisey and G K Hubler. ‘Pulsed Laser Deposition of Thin Films’. In: *Ed. DB Chrisey y G. K. Hubler. John Wiley and Sons.(USA) Cap{\’\i}tulo* 16 (1994), pp. 407–412.

[76] J T Jackson and B S Palmer. ‘Oxide superconductor and magnetic metal thin film deposition by pulsed laser ablation: a review’. In: *Journal of Physics D: Applied Physics* 27.8 (1994), pp. 1581–1594.

[77] Michael N R Ashfold et al. ‘Pulsed laser ablation and deposition of thin films.’ In: *Chemical Society reviews* 33.1 (2004), pp. 23–31.

[78] Deepika Bhattacharya, F L K Singh and P H Holloway. ‘thin fTlms interactions during pulsed laser deposition of superconducting’. In: *Journal of Applied Physics* 70.10 (1991), pp. 5433–5439.

[79] K R Singh, W O Holland and J Narayan. ‘Theoretical model for deposition of superconducting thin films using pulsed laser evaporation technique’. In: *Journal of Applied Physics* 68.13 (1990), pp. 233–247.

[80] R. Ramesh et al. ‘Epitaxial Cuprate Superconductor/Ferroelectric Heterostructures’. In: *Science* 252.5008 (May 1991), pp. 944–946.

[81] Richard F Haglund et al. *Laser Ablation and Desorption.* Vol. 30. Academic Press, 1997, pp. 475–571.

[82] Jørgen Schou, Salvatore Amoruso and James G Lunney. ‘Plume Dynamics’. In: *Laser Ablation and its Applications.* Ed. by Claude Phipps. Boston, MA: Springer US, 2007, pp. 67–95.

[83] J. Schou. ‘Physical aspects of the pulsed laser deposition technique: The stoichiometric transfer of material from target to film’. In: *Applied Surface Science* 255.10 (Mar. 2009), pp. 5191–5198.

[84] J A Venables, G D T Spiller and M Hanbucken. ‘Nucleation and growth of thin films’. In: *Reports on Progress in Physics* 47.4 (1984), p. 399.

[85] M Ohring, S Zarrabian and A Grogan. ‘The materials science of thin films’. In: *Academic Press* 31 (Dec. 1992), p. 7162.

[86] Hans-Ulrich Krebs and Olaf Bremert. ‘Pulsed laser deposition of thin metallic alloys’. In: *Applied Physics Letters* 62.19 (May 1993), p. 2341.

[87] Ian W Boyd. ‘Thin Film Growth by Pulsed Laser Deposition’. In: *Laser in der Technik / Laser in Engineering: Vortr{ä}ge des 11. Internationalen Kongresses / Proceedings of the 11th International Congress*. Ed. by Wilhelm Waidelich. Berlin, Heidelberg: Springer Berlin Heidelberg, 1994, pp. 349–359.

[88] W Prellier, Ph. Lecoeur and B Mercey. ‘Colossal-magnetoresistive manganite thin films’. In: *Journal of Physics: Condensed Matter* 13 (2001), R915.

[89] H M Christen and G Eres. ‘Recent advances in pulsed-laser deposition of complex oxides.’ In: *J. Phys.: Condens. Mat.* 20.26 (July 2008), p. 264005.

[90] N D Scarisoreanu et al. ‘Lead-free ferroelectric thin films obtained by pulsed laser deposition’. In: *Applied Physics A* 101.4 (2010), pp. 747–751.

[91] H. Zheng et al. ‘Multiferroic BaTiO3-CoFe2O4 Nanostructures’. In: *Science* 303.5658 (2004).

[92] W Prellier, M P Singh and P Murugavel. ‘The single-phase multiferroic oxides: from bulk to thin film’. In: *Journal of Physics: Condensed Matter* 17 (2005), pp. 7753–7753.

[93] G Lawes and G Srinivasan. ‘Introduction to magnetoelectric coupling and multiferroic films’. In: *Journal of Physics D: Applied Physics* 44.24 (2011), p. 243001.

[94] J.C.S. Kools and Ts Baller. ‘Gas flow dynamics in laser ablation deposition’. In: *Journal of applied Physics* 71.August 1991 (1992), pp. 4547–4556.

[95] Rajesh V Chopdekar, Elke Arenholz and Y Suzuki. ‘Orientation and thickness dependence of magnetization at the interfaces of highly spin-polarized manganite thin films’. In: *Phys. Rev. B* 79.10 (Mar. 2009), p. 104417.

[96] C. Adamo et al. ‘Effect of biaxial strain on the electrical and magnetic properties of (001) La[sub 0.7]Sr[sub 0.3]MnO[sub 3] thin films’. In: *Applied Physics Letters* 95.11 (2009), p. 112504.

[97] J Daillant and M Alba. ‘High-resolution x-ray scattering measurements: I. Surfaces’. In: *Reports on Progress in Physics* 1725.10 (Oct. 2000), pp. 1725–1777.

[98] B.L. Henke, E.M. Gullikson and J.C. Davis. *X-Ray interactions: photoabsorption, scattering, transmission, and reflection at E = 50-30,000 eV, Z = 1-92.* 1993.

[99] Max Born, Emil Wolf and A B Bhatia. *Principles of Optics: Electromagnetic Theory of Propagation, Interference and Diffraction of Light.* Cambridge University Press, 1999.

[100] R Sayers et al. 'Epitaxial growth and enhanced conductivity of an IT-SOFC cathode based on a complex perovskite superstructure with six distinct cation sites'. In: *Chem. Sci.* 4.6 (2013), pp. 2403–2412.

[101] Oliver S Heavens. 'Optical properties of thin solid films'. In: (1955).

[102] Kenneth Levenberg. 'A Method for the Solution of Certain Non-Linear Problems in Least'. In: *Quarterly of Applied Mathematics*. Vol. 2. 2. 1944, pp. 164–168.

[103] D W Marquardt. *An algorithm for least-squares estimation of non-linear parameters*. 1963.

[104] Frédéric Ott. *SimulReflec*. `http://www-llb.cea.fr/prism/programs/simulreflec/simulreflec.html`.

[105] Peter J Mohr, David B Newell and Barry N Taylor. *CODATA Recommended Values of the Fundamental Physical Constants: 2014 - Summary*. Aug. 2015.

[106] A Segmuller and A E Blakeslee. 'X-ray diffraction from one-dimensional superlattices in GaAsP crystals'. In: *Journal of Applied Crystalography* 6 (1973), p. 19.

[107] W. Sevenhans et al. 'Cumulative disorder and x-ray line broadening in multilayers'. In: *Physical Review B* 34.8 (1986), pp. 5955–5958.

[108] Charles Kittel. 'Introduction to solid state physics'. In: (1953).

[109] N Balakrishnan Norman L. Johnson Samuel Kotz. *Continuous univariate distributions. Vol.1*. 2ed. Wiley Series in Probability and Statistics. Wiley-Interscience, 1994.

[110] Izrail Solomonovich Gradshteyn and Iosif Moiseevich Ryzhik. *Table of integrals, series, and products*. Academic press, 2007.

[111] J. P. Locquet et al. 'Long-range order and lattice mismatch in metallic superlattices'. In: *Physical Review B* 38.5 (1988), pp. 3572–3575.

[112] J. P. Locquet et al. 'Discrete and continuous disorder in superlattices'. In: *Physical Review B* 39.18 (1989), pp. 13338–13342.

[113] Sameer Agarwal, Keir Mierle et al. *Ceres Solver*. `http://ceres-solver.org`.

[114] K Madsen, H B Nielsen and O Tingleff. *Methods for Non-Linear Least Squares Problems*. 2004.

PUBLICATIONS

Some results and figures have appeared previously in the following publications:

Poster presented in FÍSICA 2016 – 20ª Conferência Nacional de Física – 26º Encontro Ibérico para o Ensino da Física (September 2016), with the title: “X-ray diffraction modelling of trilayer nanostructured thin films”. J. Oliveira and B. G. Almeida.